

# Water Resources Research®

## RESEARCH ARTICLE

10.1029/2023WR035517

## Imbalances in Dissolved Elemental Export Fluxes Disclose “Hidden” Critical Zone Compartments



### Key Points:

- Imbalances between short-term and long-term estimates of element-specific chemical weathering fluxes (DEE < 1) emerge in deep saprolite
- Elements with shallow C-Q slopes showing chemostatic or enrichment behavior are likely exported in colloidal form during flushing events
- Elements with steeper C-Q slopes showing weak dilution behavior remain in re-growing biomass or are exported in particulate biogenic form

### Supporting Information:

Supporting Information may be found in the online version of this article.

### Correspondence to:

D. Uhlig,  
d.uhlig@fu-berlin.de

### Citation:

Uhlig, D., Sohrt, J., & von Blanckenburg, F. (2024). Imbalances in dissolved elemental export fluxes disclose “hidden” critical zone compartments. *Water Resources Research*, 60, e2023WR035517. <https://doi.org/10.1029/2023WR035517>

Received 6 JUN 2023  
Accepted 25 APR 2024




### Author Contributions:

#### Funding acquisition:

F. von Blanckenburg

Writing – original draft: D. Uhlig

Writing – review & editing: D. Uhlig,  
J. Sohrt, F. von Blanckenburg

D. Uhlig<sup>1,2</sup> , J. Sohrt<sup>3</sup> , and F. von Blanckenburg<sup>1,2</sup> 

<sup>1</sup>GFZ German Research Centre for Geosciences, Section Earth Surface Geochemistry, Potsdam, Germany, <sup>2</sup>Freie Universität Berlin, Institute of Geological Sciences, Berlin, Germany, <sup>3</sup>Chair of Hydrology, Albert Ludwigs University of Freiburg, Freiburg, Germany

**Abstract** In streams, short-term element-specific solute fluxes are often not balanced with long-term chemical weathering fluxes determined in the residual solids from fractional element loss and denudation rate. The ratio of both estimates—the “Dissolved Export Efficiency” (DEE)—is frequently <1, indicating deficits in the stream dissolved load. To explore the cause of the stream deficits, we performed a daily water sampling campaign for one year in a forested headwater watershed in Southern Germany. We sampled surface runoff, above-canopy and below-canopy precipitation, subsurface flow from the organic soil layer, upper, and deep mineral soil, and groundwater. Regolith samples were obtained from a drill core and revealed the weathering front to lie between 7 and 15 m depth. We found a DEE < 1 for K, Si, Al, Fe. These elements are characterized by shallow slopes in C-Q relationships, and the imbalances were found to originate in the deep saprolite. Their export pathway potentially includes “hidden” Critical Zone compartments or fluxes, presumably unsampled colloids that are exported preferentially during rare flushing events with stochastic temporal distribution. The DEE of nutritive elements like Ca, Mg, and P is also <1. These elements are characterized by steeper C-Q slopes, and their imbalance can be explained by deep nutrient uptake followed by nutrient retainment in re-growing forest biomass or export in plant debris. The collective evidence for these imbalances, including previous evidence from metal stable isotopes, suggests that the deep Critical Zone represents the location for chemical or biogenic retention and release of solutes.

**Plain Language Summary** Mineral dissolution by chemical weathering produces solutes in the weathering zone that are eventually exported by streams. Yet, often an imbalance between element-specific solute export fluxes in stream water and element-specific chemical weathering fluxes determined from residual solids in the weathering zone is apparent. This imbalance is expressed as a deficit in the stream dissolved load. To explore the origin of this deficit, we performed a daily water sampling campaign for one year in a forested watershed in Southern Germany. We studied concentration–discharge relationships and quantified solute fluxes in stream- and groundwater. A comparison of solute fluxes in stream water with chemical weathering fluxes integrating mineral dissolution over the whole weathering zone revealed indeed deficits in the stream dissolved load. These deficits originate in deep isovolumetrically weathered bedrock (saprolite). The elements K, Si, Al, and Fe, which show invariant concentration changes with increasing discharge, may follow a “hidden” export pathway involving colloids that are only mobilized and exported during rare flushing events that were missed during this study’s sampling period. Deficits of nutrients (Ca, Mg, P), which show dilution behavior with increasing discharge, can be explained by deep nutrient uptake and retention in growing forest biomass or plant litter erosion.

## 1. Introduction

The chemical composition of stream water results from intertwined hydrological and biogeochemical element cycling between the top of the tree canopy, regolith, unweathered parent bedrock and the base of the groundwater table—the Critical Zone. Stream solute concentrations are set by processes like mineral dissolution and precipitation (Gaillardet et al., 1999; Kump et al., 2000; White & Blum, 1995), water flow (Johnson et al., 1969), nutrient uptake by organisms (Herndon et al., 2015; Johnson et al., 1969; Mulholland, 1992; Sullivan et al., 2019; Vitousek, 1977), atmospheric inputs (Gibbs, 1970), cation exchange reactions (Clow & Mast, 2010), and in-stream processes (Baronas et al., 2017) like nutrient utilization by periphyton (Sohrt et al., 2019) and sorption processes (Tipper et al., 2021), amongst others.

© 2024. The Authors.

This is an open access article under the terms of the [Creative Commons Attribution License](https://creativecommons.org/licenses/by/4.0/), which permits use, distribution and reproduction in any medium, provided the original work is properly cited.

The integrated sum of these controls emerges in the form of element-specific solute export fluxes, that after correction for atmospheric inputs, are commonly interpreted to represent element-specific chemical weathering fluxes ( $W$ , e.g., in  $\text{g m}^{-2} \text{yr}^{-1}$ ). Accordingly, weathering rates are estimated from river gauging by calculating the product of stream discharge ( $Q$ , e.g., in  $\text{l s}^{-1}$ ) and solute concentration ( $C$ , e.g., in  $\text{mg l}^{-1}$ ) (e.g., Gaillardet et al., 1999; Moon et al., 2014). The fluxes resulting from this approach represent the time interval of river gauging, typically  $10^1$ – $10^2$  yrs. A complementary estimate of these “short-term” element-specific chemical weathering fluxes derived from river gauging are “long-term” estimates of element-specific chemical weathering fluxes ( $10^3$ – $10^5$  yr integration timescale) derived from regolith. Regolith-derived weathering fluxes are calculated from the product of the fractional loss of element  $X$  in regolith relative to unweathered parent bedrock, and the cosmogenic nuclide-derived total denudation rate of regolith (e.g., Hewawasam et al., 2013) that is, at steady state, the formation rate of regolith from bedrock. However, in newer studies the comparison of short-term estimates of chemical weathering fluxes with their long-term counterpart increasingly reveal imbalances. These imbalances have been found by means of element chemical (von Blanckenburg et al., 2021; Charbonnier et al., 2022; Frings et al., 2021; Kim et al., 2018) and metal stable isotope-based mass balances (von Blanckenburg et al., 2021; Bouchez & von Blanckenburg, 2021; Cai et al., 2024; Charbonnier et al., 2020; Schuessler et al., 2018; Uhlig et al., 2017). These imbalances persist even after correction for timescale effects, potentially arising from variations in discharge with time, using a “conservative” element such as Na that is neither a nutrient to trees nor a major constituent of clay or other secondary solids (von Blanckenburg et al., 2021; Schuessler et al., 2018; Uhlig et al., 2017). As short-term fluxes are lower than long-term regolith release fluxes, the authors of the aforementioned three studies suggested that the differences in fluxes represent true imbalances and introduced the term “Dissolved Export Efficiency” (DEE) to account for a deficit in export of a given element over its release by weathering.

One speculation put forward to explain the imbalance is the subsurface export of colloidal-sized particles (Bern et al., 2011, 2015; Kretzschmar et al., 1995; Ma et al., 2015; Sullivan et al., 2016) that is not accounted for in the dissolved riverine export fraction. This speculation seems reasonable, when considering that most of the operationally defined dissolved riverine export of Al and Fe is not truly dissolved but is rather dominated by colloids (Mills et al., 2017). An alternative explanation put forward more recently is element uptake by plants and storage or export in plant debris, thus preventing an element, once released from saprolite, to be exported in the dissolved form by rivers (von Blanckenburg et al., 2021; Schuessler et al., 2018; Uhlig et al., 2017).

The evaluation of subsurface colloidal-sized particle export requires an analysis of the relationship between solute concentration and discharge for the elements in question. This relationship is typically described by a power law function in the form of  $C = a \cdot Q^b$  (Godsey et al., 2009), where the constant  $a$  represents the intercept at  $Q = 1$  and the power-law exponent  $b$  ( $b$ -value) represents the slope. Two end member C-Q relationships can be defined: “chemostatic,” and “chemodynamic” behavior. Whereas chemostasis describes solute concentrations that are close to invariant over a range in discharge of several orders of magnitude, chemodynamic behavior describes either a decrease in concentration (dilution) or increase in concentration (enrichment) with increasing discharge (Godsey et al., 2009, 2019; Kirchner & Neal, 2013).

Chemostatic behavior was found across the globe for geogenic (weathering-derived) elements such as Ca, Mg, Na, Si (Godsey et al., 2009) and nutritive elements such as geogenic P and atmospheric N (Basu et al., 2010; Musolff et al., 2015; Thomas et al., 2016; Thompson et al., 2011) in a variety of climatic, geomorphic, or lithologic regimes (Godsey et al., 2009, 2019; Ibarra et al., 2016; Moon et al., 2014; Torres et al., 2015; Zakharova et al., 2005). A multitude of potential explanations were put forward toward the origin of chemostatic behavior. Two main processes were hypothesized. First, water transit times through the porous subsurface are sufficiently low to allow for chemical equilibrium (Ibarra et al., 2016; Maher, 2010, 2011; Maher & Chamberlain, 2014) between the dissolution and formation of poorly crystalline aluminosilicates (Clow & Mast, 2010). Second, the mobilization and transport of pre-event water (e.g., pore water being high in solute concentration) by event water (e.g., rainwater being low in solute concentration) into the stream sustains solute concentrations of stream water (e.g., Cartwright, 2020; Johnson et al., 1969). Mobilized elements are either homogeneously distributed in the catchment's pore water (Herndon et al., 2015), stored in shallow soil of the riparian zone (Pacific et al., 2010), or in the easily exchangeable fraction in soil (Bao et al., 2017; Clow & Mast, 2010).

Chemodynamic behavior can yield positive C-Q slopes (enrichment), where concentrations are low at low flow conditions and high at high flow conditions. This behavior has been attributed to a hydrologic connectivity

between topsoil and the stream, which is re-established after a preceding period of low flow (Pacific et al., 2010). This connectivity is attained through partial saturation of flow paths within the soil and activation of the riparian zone around the channel. Thus, truly dissolved organic compounds (e.g., DOC, DON) and nutritive elements (e.g., P), colloids, and elements complexed with organic matter (e.g., Al, Fe, Mn) are mobilized (Pacific et al., 2010; Seibert et al., 2009; Trostle et al., 2016). Chemodynamic behavior can also yield negative C-Q slopes (dilution), where concentrations are high at low flow conditions and low at high flow conditions. This behavior has been found, when the catchment's pore water solute store becomes rapidly depleted during infiltration events (Herndon et al., 2015; Hoagland et al., 2017), or, if fluid residence times in the regolith are short enough for groundwater solute concentrations to get diluted by event water during periods of high rainfall (Bao et al., 2017; Miller et al., 2016). Dilution behavior also occurs at high flow conditions, when flow paths do no longer intersect with weatherable minerals (Winnick et al., 2017).

In this paper we (a) explored the spatiotemporal evolution of C-Q relationships on a daily basis, (b) assessed the role of C-Q relationships on the imbalance found between short-term and long-term estimates of element-specific chemical weathering fluxes, expressed by a Dissolved Export Efficiency (DEE) < 1, and (c) resolved the depth interval over which deficits in the stream dissolved load emerged. In doing so, we built on previous work at the Conventwald site (Black Forest, Germany). Critical Zone work at this site was used to develop new concepts of nutrient cycling and nutrient sourcing in the “organic nutrient cycle” and the “geogenic nutrient pathway” (Uhlig et al., 2020; Uhlig & von Blanckenburg, 2019). Further work focused on the (hydro-)geochemical characterization of dissolved P (Sohrt et al., 2019), and colloids (Gottselig et al., 2020). A study on Mg stable isotopes showed that Mg in groundwater and discharge was strongly buffered by the exchangeable pool (Cai et al., 2022). A further study on Li stable isotopes suggested a “hidden export pathway” of secondary formed Li-bearing fine particles from the Critical Zone (Cai et al., 2024). For the present study we performed daily water sampling of six different hydrological compartments, namely above-canopy precipitation (bulk precipitation (BP) including rainwater, snow and fog water), below-canopy precipitation (throughfall (TF)), subsurface flow from three distinct soil horizons (organic layer (SF1), upper mineral soil (SF2), deep mineral soil (SF3)), groundwater (GW), creek water (CW) and spring water (SW) at two neighbored first order headwater catchments over the course of one year. We quantified short-term element-specific chemical weathering fluxes and compared them with its long-term counterpart determined in Uhlig and von Blanckenburg (2019) from cosmogenic nuclides to assess net elemental losses from or gains to the Conventwald and found indirect evidence for colloid-bound export.

## 2. Study Site

This study was conducted in the Conventwald (48°02'0 N, 7°96'0 E) situated in the Black Forest, Germany, which is close to the Strengbach catchment (Vosges Mountains, France) that belongs to the OZCAR Critical Zone Observatories (Gaillardet et al., 2018). The study area comprises two neighboring headwater catchments (Figure 1): the “spring catchment” (0.077 km<sup>2</sup>) and the “creek catchment” (0.086 km<sup>2</sup>). Whereas the creek catchment contains a channel bed and thus features surface runoff, the spring catchment is sampled at its spring and thus samples exclusively subsurface water. The mean annual temperature is 7.9°C (Eichhorn et al., 2016), the mean annual precipitation is 1,395 mm (Eichhorn et al., 2016), and the mean elevation is 790 m above sea level. Both catchments are south-facing but the slopes differ between the creek catchment (20°) and the spring catchment (17°). The vegetation comprises European beech (*Fagus sylvatica*) and Norway spruce (*Picea abies*) of about 130 years of average age (Lang et al., 2017). Felsic paragneiss is underlying both catchments. The normative mineral assembly of the paragneiss comprises mainly plagioclase (anorthite component of 27 vol.-% and albite component of 25 vol.-%), K-feldspar (12 vol.-%), quartz (12 vol.-%), pyroxene (9 vol.-%), cordierite, biotite, hornblende, and chlorite (Uhlig & von Blanckenburg, 2019). Even though the Conventwald sites were not glaciated throughout the Quaternary, periglacial slope deposits developed, providing the source material for pedogenesis. The soil type of both study sites is a Hyperdystric skeletal folic Cambisol (IUSS Working Group WRB, 2015) with about 70% rock fragments >2 mm within the top 100 cm of soil, and a moor-like moder organic layer atop (Lang et al., 2017). Weathered bedrock and unweathered parent bedrock were found at 7 and 15 m depth, respectively, as identified during a drilling campaign described in Uhlig and von Blanckenburg (2019).

Given that the study area has been monitored since three decades by the International Co-operative Program on assessment and monitoring of air pollution effects on forests (ICP Forests), the study area was equipped by the

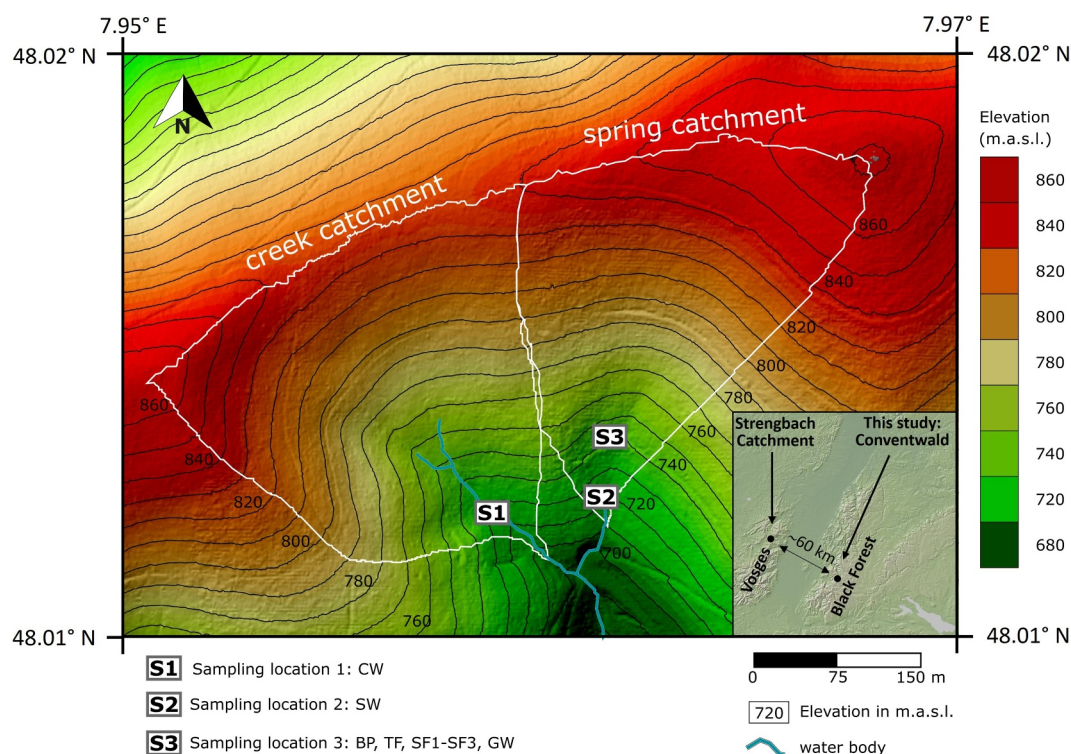


**Figure 1.** Map of the Conventwald sampling locations. Shown are the two neighboring headwater catchments: spring catchment and creek catchment. Symbols mark sampling locations of bulk precipitation (BP), throughfall (TF), subsurface flow (SF1-SF3), groundwater (GW), spring water (SW), and creek water (CW).

“Forstliche Versuchsanstalt Baden-Wuerttemberg,” Freiburg, Germany (hereafter termed “FVA”), with above- and below canopy precipitation collectors, soil moisture sensors and a V-notched discharge weir at the outlet of the creek catchment. Additionally, the spring catchment was equipped by GFZ-Potsdam with a groundwater well (filter line from 7 to 16 m depth), and by the University Freiburg with a V-notched discharge weir directly at the outlet of the spring catchment and collectors of subsurface flow at three depth intervals covering the soil layers Ah + Bw (0–15 cm, hereafter “top layer (SF1)”), Bw (15–150 cm, hereafter “intermediate layer (SF2)”) and Bw + Cw (150–320 cm, hereafter “basal layer (SF3)”). A glossary of sampling stations is provided in Table 1. Detailed information on the construction for subsurface water flow sampling is available in Bachmair and Weiler (2012) and Sohrt et al. (2019). The total denudation rate amounts to  $125 \text{ t km}^{-2} \text{ yr}^{-1}$  (Uhlig & von Blanckenburg, 2019) and was quantified from in situ cosmogenic  $^{10}\text{Be}$  concentrations measured on bedload sediment sampled at the catchment outlet.

**Table 1**  
Glossary of Sampling Stations

ID	Sampling station	Description
BP	Bulk precipitation	Above-canopy precipitation including rainfall, snow, fog water
TF	Throughfall	Below-canopy precipitation
SF1	Subsurface flow (0–15 cm)	Subsurface flow from the top layer (organic soil)
SF2	Subsurface flow (15–150 cm)	Subsurface flow from the intermediate layer (upper mineral soil)
SF3	Subsurface flow (150–320 cm)	Subsurface flow from the basal layer (deep mineral soil)
GW	Groundwater (700 cm)	Subsurface flow sampled from aquifer
CW	Creek water	Surface runoff from creek
SW	Spring water	Subsurface water sampled at spring outlet

### 3. Methods

#### 3.1. Sampling

Sampling was carried out over the course of one year from 01.03.2015 to 25.02.2016. Groundwater, creek water, and spring water were sampled at a daily resolution. Subsurface flow was only sampled on days that were preceded by precipitation events. Sampling was carried out at midnight by automatic samplers (self-construction, University of Freiburg, Hydrology). These samplers contained 30 pre-cleaned polypropylene bottles of 150 ml volume, which allowed sample collection on up to ten consecutive days with three replicates taken each day. At a bi-weekly resolution, bulk precipitation and throughfall were sampled in precipitation collectors and transferred directly in the field into 100 ml pre-cleaned polypropylene bottles. Samples from all locations were collected every three to four days, acidified after filtration through 0.8  $\mu\text{m}$  membranes (Supor 800, Pall Laboratories) to pH 3 with quartz glass distilled 14 M  $\text{HNO}_3$  and shipped to GFZ-Potsdam in 15 ml polypropylene bottles, which were soaked for about two days each in 1 M  $\text{HNO}_3$ , 1 M  $\text{HCl}$  and deionized water (Milli-Q water, 18.2 M $\Omega$ ). Samples were stored at 4°C prior to analyses. To meet the requirements of project partners participating in this sampling campaign, the pore size of the filters was 0.8  $\mu\text{m}$ , which exceeded the commonly used pore size of 0.20  $\mu\text{m}$  or 0.45  $\mu\text{m}$ .

#### 3.2. Analytical Methods

Analytical procedures were mainly carried out at the Helmholtz Laboratory for the Geochemistry of the Earth Surface (HELGES, von Blanckenburg et al. (2016)). Prior to concentration analyses, dilution of samples, reference materials and in-house standards, and preparation of calibration standards were carried out gravimetrically in an ISO class 6 clean laboratory. A comprehensive method description for the analyses of major and trace element concentrations is published in Schuessler et al. (2016) and Sohr et al. (2019). Briefly, samples were diluted with 0.3 M  $\text{HNO}_3$  containing 1 mg  $\text{g}^{-1}$  Cs and the concentrations of major elements (Ca, K, Mg, Na, S, Si) and trace elements (Al, Ba, Cr, Cu, Li, Fe, Sr, Zn) were measured with an inductively coupled plasma optical spectrometer (ICP-OES, Varian 720ES) by external calibration with matrix-matched calibration standards. Analytical uncertainties were obtained from repeat analyses of four standard reference materials (National Research Council of Canada (SLRS-5), National Institute of Standards and Technology (SRM 1640a), and U.S. Geological Survey (M-212, T187)) as well as synthetic in-house standards resembling a typical river water matrix containing major constituents (Ca, K, Mg, Na, S, Si) and trace constituents (Cu, Fe, Ni, P, Ti, Zn) prepared from single element standard solutions (Merck Millipore). Relative uncertainties are listed in Table S7 (in data publication Uhlig et al. (2024)) and were better than 5% for major and better than 10% for trace elements.

Phosphorus concentrations (previously published in Sohr et al. (2019)) were measured without dilution by inductively coupled plasma mass spectrometry (ICP-MS, Element2, Thermo Fischer Scientific) in medium resolution ( $m/z \approx 4,000$ ) and with external calibration. Tests prior to the measurements showed that matrix-matched calibration was not needed, since no significant matrix effects were observed in the concentration range of the major elements. Accuracy and precision were assessed using two standard reference materials (SLRS-5 and M212) and in-house standards with river water matrix. The relative uncertainty of P analyses is listed in Table S7 (in data publication Uhlig et al. (2024)) and is better than 10%.

Concentrations of total dissolved carbon (C), dissolved inorganic carbon (DIC), dissolved organic nitrogen (DON), and chloride (Cl) were also previously published in Sohr et al. (2019). Concentrations of C, DIC, and DON were measured with a Shimadzu Vcfn analyzer. Given that all concentrations of DIC were below the limit of detection of 50  $\mu\text{g l}^{-1}$ , total dissolved carbon corresponds to dissolved organic carbon (DOC). Chloride was measured with an ion chromatograph (790 Personal IC, Metrohm) at the Chair of Soil Ecology, University of Freiburg.

#### 3.3. Data Evaluation Methods

##### 3.3.1. Concentration-Discharge Relationships

Two metrics were used to explore the dependence of solute concentration (C) on discharge (Q) in spring water and creek water. First, the fitted  $\log(C)$ - $\log(Q)$  power law slope (b-value) was used to define chemostatic behavior

( $-0.1 < b < 0$ ), and chemodynamic behavior comprising dilution behavior ( $b < -0.1$ ) and enrichment behavior ( $b > 0$ ) (Godsey et al., 2009; Herndon et al., 2015; Hoagland et al., 2017). To estimate the uncertainty (standard error) and statistical significance (p-value) of the b-value, the data analysis tool “regression” from Microsoft Excel 2016 was applied to the logarithmized data.

Second, the ratio of the coefficient of variation ( $CV_C/CV_Q$ , Equation 1), which is the standard deviation ( $\sigma$ ) of concentration or discharge normalized by its mean value ( $\mu$ ), was used to define chemostatic behavior. For two reasons the ratio  $CV_C/CV_Q$  is better suited to determine whether elements truly show chemostatic behavior than the C-Q relationship alone (Thompson et al., 2011). On the one hand, a b-value of zero is no evidence for the absence of small variations in concentration. On the other hand, conventional metrics such as the coefficient of determination ( $R^2$ ) or the statistical significance (p-value) describing the goodness of the power law C-Q fit become uninformative, when the b-value approaches zero. Chemostatic behavior can be considered when  $CV_C/CV_Q \ll 1$  (Thompson et al., 2011) and chemodynamic behavior can be considered when  $CV_C/CV_Q$  is not  $\ll 1$  (Musolff et al., 2015).

$$\frac{CV_C}{CV_Q} = \frac{\mu_Q \cdot \sigma_C}{\mu_C \cdot \sigma_Q} \quad (1)$$

### 3.3.2. End Member Mixing Analysis

The relative proportions of different water compartments contributing to discharge were disentangled using an end member mixing analysis (EMMA). The EMMA was described in detail in Sohrt et al. (2019) and used solute concentrations presented in this study as input parameters from three end members: Groundwater, subsurface flow from the top layer (SF1, Table 1) and from the combined intermediate and basal layer (SF2 and SF3, Table 1). Annual average element concentrations of Ca, Cl, DOC, K, Mg, Na, S and Si from all water compartments were processed with the software package EMMAgeo in the R Environment (Dietze & Dietze, 2013). Then, the model was calibrated to time series data using element concentrations of spring water. Data from the basal layer SF3 was combined with data from the intermediate layer SF2 because of the limited number of samples from SF3.

### 3.3.3. Geochemical Modeling

Mineral saturation indices (SI, Equation 2, where IAP is the ion activity product and  $K_{eq}$  is the equilibrium constant for the reaction) of primary minerals resembling as best as possible the mineralogical composition of parent bedrock and potential secondary solids were calculated for spring water, creek water, and groundwater using the software program PhreeqC—version 3 (Parkhurst & Appelo, 2013). Thermodynamic constants included in the geochemical database wateq4f were used. Input parameters comprised concentrations of the anion  $Cl^-$  published in Sohrt et al. (2019), as well as all major elements and trace elements measured in this study (Tables S4–S6 in data publication Uhlig et al. (2024)) except Cr, Li, Mn. These three elements were excluded because their concentrations were mainly below the limit of quantification. Input parameters on basic water quality comprised measured water temperature, a default value of the negative logarithm of the conventional electron activity (pe: 4), and pH. Because pH values were not measured during our sampling period but were measured bi-weekly by the FVA in previous years, the pH value was set to default values representing a minimum (pH 6) and a maximum (pH 7) pH value in creek water. For groundwater, no time series of pH values are available. However, the pH of groundwater was measured prior to the sampling period and yielded a value of 8. Allowing the pH to vary by one pH value, the pH of groundwater was set to default values of 7.5 and 8.5. Phlogopite was used as end member for the solid solution series of biotite. Saturation indices of zero indicate minerals are at chemical equilibrium with the solution. Positive saturation indices indicate supersaturation of the solution and hence formation of secondary solids. Negative saturation indices point to undersaturation of the solution and hence to mineral dissolution.

$$SI = \log\left(\frac{IAP}{K_{eq}}\right) \quad (2)$$

### 3.4. Fluxes

#### 3.4.1. Annual Solute Fluxes

Solute fluxes of a watershed can be categorized into input fluxes, throughflow fluxes, and export fluxes. Annual solute input fluxes of element X comprise atmospheric wet deposition (bulk precipitation,  $\text{Dep}_{\text{BP}}^{\text{X}}$ ) and the dissolved fraction of dry deposition (dust,  $\text{Dep}_{\text{dust}}^{\text{X}}$ ) that is sourced from external locations such as deserts and arable soils.  $\text{Dep}_{\text{BP}}^{\text{X}}$  was determined from Equation 3, where  $[X]_i$  is the solute concentration of element X of day i, and  $F_i$  is the amount of bulk precipitation in  $\text{l m}^{-2}$  of day i. The concentrations of K, Mn, Na, Si and Sr were often below the limit of detection and annual averages were used in these cases. In addition to  $\text{Dep}_{\text{BP}}^{\text{X}}$  derived from the 1-year data set of this study, the long-term (1992–2019) average of  $\text{Dep}_{\text{BP}}^{\text{X}}$  (termed here  $^*\text{Dep}_{\text{BP}}^{\text{X}}$ ) was calculated from monitoring data of the FVA.

$$\text{Dep}_{\text{BP}}^{\text{X}} = \sum_{i=1}^n [X]_i \cdot F_i \quad (3)$$

$\text{Dep}_{\text{dust}}^{\text{X}}$  was determined from Equation 4, where  $F_{\text{dust}}$  is the total dust deposition rate and  $[X]_{\text{UCC}}$  is the concentration of element X in the upper continental crust (UCC). In the absence of monitoring data on dust deposition rates, minimum and maximum values of  $F_{\text{dust}}$  were taken from global dust deposition maps provided by Jickells et al. (2005) and Zender et al. (2003). At our study site, dust deposition rates amount to a minimum of  $2,000 \text{ mg m}^{-2} \text{ yr}^{-1}$  and a maximum of  $5,000 \text{ mg m}^{-2} \text{ yr}^{-1}$ . Element concentrations of UCC were taken from Taylor and McLennan (1995).

$$\text{Dep}_{\text{dust}}^{\text{X}} = [X]_{\text{UCC}} \cdot F_{\text{dust}} \quad (4)$$

Annual solute throughflow fluxes of element X comprise throughfall ( $\text{Dep}_{\text{TF}}^{\text{X}}$ ), subsurface flow ( $W_{\text{SF}}^{\text{X}}$ ) and groundwater ( $W_{\text{GW}}^{\text{X}}$ ).  $\text{Dep}_{\text{TF}}^{\text{X}}$  was determined from Equation 5, where  $[X]_i$  is the solute concentration of element X of day i, and  $F_i$  is the amount of throughfall in  $\text{l m}^{-2}$  of day i. The concentration of Sr was often below the limit of detection and annual averages were used in this case.

$$\text{Dep}_{\text{TF}}^{\text{X}} = \sum_{i=1}^n [X]_i \cdot F_i \quad (5)$$

$W_{\text{SF}}^{\text{X}}$  was determined for the top layer (0–15 cm; SF1) and the combined intermediate and basal layer (15–320 cm; SF2 and SF3) from Equation 6.  $[X]$  is the mean annual solute concentration. Because water flow could not be measured in subsurface flow, its daily fractional contribution ( $f_i$ ) to stream discharge was estimated from the EMMA (Section 3.3.2) and multiplied with the catchment area (A) normalized daily discharge ( $Q_i$ ). Even though daily sampling was attempted, for technical reasons some samples could not be taken. The resulting data gaps were filled by interpolation.

$$W_{\text{SF}}^{\text{X}} = [X] \cdot \sum_{i=1}^n f_i \frac{Q_i}{A} \quad (6)$$

$W_{\text{GW}}^{\text{X}}$  was determined from Equation 7, where  $[X]_i$  is the solute concentration of element X of day i. Similar to  $W_{\text{SF}}^{\text{X}}$ , water flow of groundwater could not be measured. Instead, its fractional contribution to stream discharge ( $f_i$ ) was multiplied with the catchment area (A) normalized daily discharge ( $Q_i$ ). Similar to  $W_{\text{SF}}^{\text{X}}$ , data gaps were filled by interpolation.

$$W_{\text{GW}}^{\text{X}} = \sum_{i=1}^n [X]_i \cdot f_i \frac{Q_i}{A} \quad (7)$$

Annual solute export fluxes comprise spring water ( $W_{\text{SW}}^{\text{X}}$ ) and creek water ( $W_{\text{CW}}^{\text{X}}$ ).  $W_{\text{SW}}^{\text{X}}$  or  $W_{\text{CW}}^{\text{X}}$  was determined from Equation 8, where  $[X]_{\text{SW}}$  or  $[X]_{\text{CW}}$  is the solute concentration of element X of day i in spring water or creek

water, and  $Q_i$  is daily discharge of the catchment area  $A$ . Because the water balance from Sohr et al. (2019) indicates that surface discharge of the spring reflects only about one fourth of the total discharge, spring surface discharge was corrected for its corresponding subsurface contribution. In spring and creek water the concentrations of the trace elements Fe, Mn and Al were often below the limit of detection. For these elements the fluxes were estimated from annual average element concentrations and yearly discharge.

$$W_{SW \text{ or } CW}^X = \sum_{i=1}^{365} [X]_{SW \text{ or } CW} \cdot \frac{Q_i}{A} \quad (8)$$

Given that the sampling campaign was carried out in a relatively dry year,  $W_{GW}^X$  and  $W_{CW}^X$  were also determined to represent the long-term hydrological condition at the Conventwald and were labeled with an asterisk. Thus,  $W_{GW}^X$  (Equation 9) and  $*W_{CW}^X$  (Equation 10) include the 2004 to 2013 average of creek discharge ( $Q_{\text{mean}}$  in  $l \text{ s}^{-1}$ ) amounting to  $3.5 \pm 2.8 \text{ l s}^{-1}$  (1SD) provided by the FVA. In Equation 9,  $f_{\text{mean}}$  is the annual average of the fractional contribution of groundwater to stream discharge amounting to 45%, and  $[X]_{\text{mean}}$  is the average annual solute concentration of groundwater. In Equation 10,  $[X]_{C-Q}$  is the solute concentration of element X in creek water at  $Q_{\text{mean}}$  and was calculated from the equations of the power law regression lines shown in Figure S1 in Supporting Information S1.

$$*W_{GW}^X = [X]_{\text{mean}} \cdot f_{\text{mean}} \frac{Q_{\text{mean}}}{A} \quad (9)$$

$$*W_{CW}^X = [X]_{C-Q} \frac{Q_{\text{mean}}}{A} \quad (10)$$

### 3.4.2. Millennial-Scale Weathering Fluxes

The element-specific chemical weathering flux ( $W_{\text{regolith}}^X$ ) provides the time-integrated dissolution flux of element X from primary minerals minus the incorporation flux of X into secondary minerals and (oxy-) hydroxides formed in the regolith.  $W_{\text{regolith}}^X$  is inferred from the total denudation flux ( $D$ ) measured by in situ cosmogenic  $^{10}\text{Be}$ , the fractional loss of element X relative to bedrock as expressed by the mass transfer coefficient ( $\tau_{Zr}^X$ ) and the concentration of element X in unweathered parent bedrock (Equation 11). All data were sourced from Uhlig and von Blanckenburg (2019). Specifically, average  $\tau_{Zr}^X$ -values from 0 to 7 m depth were used, unless profiles feature depletion-enrichment patterns, as, for example, for Al, Fe, Mn, P, Si, Zn. In this case, average  $\tau_{Zr}^X$ -values from below the enrichment horizons from 1.4 to 7.0 m depth were used.

$$W_{\text{regolith}}^X = D \cdot [X]_{\text{rock}} \cdot (-\tau_{Zr}^X) \quad (11)$$

whereas  $W_{\text{regolith}}^X$  integrates the elemental loss from the entire weathering zone, the element-specific chemical weathering flux can also be quantified separately for individual regolith intervals, for example, for soil, saprolite and weathered bedrock. Because the soil is affected by atmospheric inputs (addition profiles, Brantley and Lebedeva (2011)) and the redistribution of elements through nutrient uplift (biogenic profile, Brantley and Lebedeva (2011)) and secondary mineral formation (depletion-enrichment profile, Brantley and Lebedeva (2011)), we limit the element-specific chemical weathering flux estimation for individual regolith intervals here to the saprolite ( $W_{\text{saprolite}}^X$ , Equation 12). A bias is not introduced as the saprolite (3–7 m depth) is free of periglacial slope deposits.  $W_{\text{saprolite}}^X$  was calculated by using weathered bedrock as parent material. For  $W_{\text{saprolite}}^X$  average element concentrations of weathered bedrock (7–15 m depth) and average  $\tau_{Zr}^X$ -values from saprolite (3–7 m depth) were used in Equation 12.

$$W_{\text{saprolite}}^X = D \cdot [X]_{\text{weathered rock}} \cdot (-\tau_{Zr}^X) \quad (12)$$



## 4. Results and First-Order Interpretation

### 4.1. Hydrological Conditions

The hydrological conditions were described in Sohrt et al. (2019) and are only briefly summarized here: Springtime and summer until June 2015 were relatively wet allowing soil moisture, groundwater level and stream discharge to respond rapidly to precipitation events. A pronounced dry period affected the Conventwald from June 2015 to November 2015. During this period, the groundwater level gradually declined by 0.4 m from 7.7 to 8.1 m depth. From November 2015 to February 2016, intense and frequent precipitation events caused a rewetting period during which the groundwater level increased by 1.6 m from 8.1 to 6.3 m depth. With 1,118 mm precipitation the sampling year was a relatively dry year—about 25% below the average of 1,395 mm (1981–2010, Eichhorn et al. (2016)).

The results from the EMMA (Tables S4 and S5 in data publication Uhlig et al. (2024)) showed that during the high flow period, spring and creek discharge were mainly fed by subsurface water from the intermediate and basal layer (SF2 and SF3, groundwater contribution 5%–10%). During low flow periods, groundwater contributed 75%–95% of spring discharge and 65%–85% of creek discharge (when applying the EMMA to the creek too). The contribution of subsurface flow from the top layer (SF1) was <<0.01%–5%—a negligible contribution to discharge.

### 4.2. Distribution and Seasonal Variation of Solute Concentrations

The entire data set of major and trace element concentrations is provided in Tables S1–S6 (in data publication Uhlig et al. (2024)), available in the open access data publication published in Uhlig et al. (2024), and average concentrations at different flow regimes and annual average concentrations are given in Table S1 in Supporting Information S1. Daily concentrations of all water compartments are shown in Figures S2 to S4 in Supporting Information S1 and average concentrations at different flow regimes are shown in Figure S5 in Supporting Information S1. We only briefly described them here as viewed from the perspective of a virtual raindrop on its route into (input), through (throughflow) and out (output) of the watershed.

Solute concentrations of bulk precipitation (BP) were highest for the major elements Ca and Na, and the trace element Zn. Seasonal variations were only found for Al, Ca and Mg concentrations, which are significantly ( $p \leq 0.05$ , Wilcoxon-Mann-Whitney test) higher in summer than in other seasons. This result is consistent with Saharan dust deposition events in southern Germany, which, according to the Deutscher Wetterdienst, peaked in July 2015 during our sampling period. Also, assuming seawater is the ultimate source of rainwater,  $[X]/[Cl]$  of BP exceeding those of seawater by up to six orders of magnitude (Figure S6 in Supporting Information S1) suggest substantial, non-seawater derived inputs to the Conventwald. Apart from long-distance traveled desert dust, such inputs may be of anthropogenic origin (e.g., agricultural, or industrial aerosols).

When bulk precipitation passes through the canopy, the most substantial concentration increases in throughfall were found for DON (~50-fold), P (>10-fold), and K (~7-fold). Throughout springtime and summer, increasing solute concentrations in throughfall were found for P, major elements (except Na, S), trace elements (Ba, Cu, Zn) and organic compounds (DOC, DON). This seasonal trend is visible in subsurface flow of the organic layer (SF1) too and disappeared toward the basal layer (SF3). When annual average concentrations of subsurface flow were evaluated, the following depth-dependent trends in subsurface flow from SF1 to SF3 were found: No substantial variation with depth was found for Cl and Si, suggesting conservative behavior. Concentrations increased with depth for Na and S, suggesting net mineral dissolution. Concentrations decreased with depth for the remaining elements, which was most pronounced for nutritive elements (DOC, P, K). This decrease suggests nutrient uptake by plants, adsorption, or complexation with organic matter and inorganic soil constituents. The depth-dependent trends from SF1 to SF3 continued further down to groundwater (GW) except for Ca, Mg and Sr concentrations that are much higher in GW than in the subsurface basal layer. When the solutes arrived in the creek or spring, their seasonal trends were, apart from P, similar in both catchments. Two general patterns emerged. Steady concentrations throughout the year were found for Si, Na, K, and Cl, suggesting chemostatic behavior. Decreasing concentrations were found for Ca, Mg, S, Ba, Sr and Zn during precipitation events suggesting dilution effects. However, concentrations returned to pre-precipitation concentrations or exceeded these during dry periods. In contrast, P showed opposed trends when comparing spring water (SW) with creek water (CW), which may be attributed to in-stream processes (Sohrt et al., 2019).

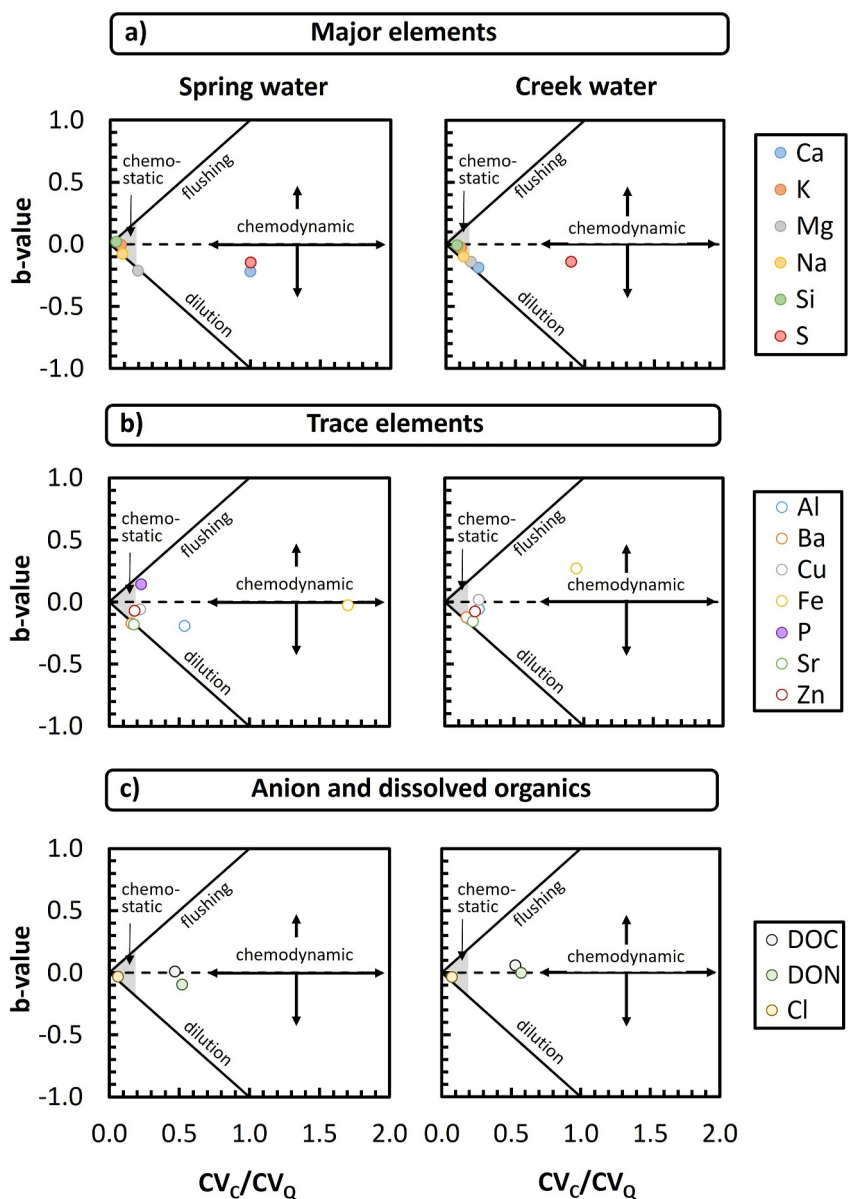


**Figure 2.** Graphical representation of concentration (C)—discharge (Q) relationships in spring water (panel a) and creek water (panel b). The b-value represents the power law slope in the C-Q space (Section 3.3.1) and the ratio  $CV_C / CV_Q$  represents the ratio of the coefficient of variation (Section 3.3.1, Equation 1).

### 4.3. Concentration—Discharge Relationships

Concentration (C)—discharge (Q) relationships are shown for spring (SW) and creek water (CW) in Figure 2 (b-value vs.  $CV_C / CV_Q$ ) and in Figure S6 in Supporting Information S1 (C vs. Q). Evaluation of the C-Q slopes (b-values, Table 2) and the ratio of the coefficient of variation in C and Q ( $CV_C / CV_Q$ , Table 2) in both catchments showed chemostatic behavior for K, Na, Si, (Al), Cu, (Fe), Zn, Cl; dilution behavior for Ca, Mg, S, (Al), Ba, (P), Sr; and enrichment behavior for Si, (P), Cu, (Fe), DOC (elements shown in brackets indicate that data stem from only one catchment). Apart from P, b-values are consistently higher in creek water than in water discharged at the spring. On the one hand, this feature could be attributed to distinct characteristics of the hyporheic zone (Hoagland et al., 2017) as the spring, unlike the creek, lacks a stream channel. On the other hand, different b-values among the spring and the creek could be the result of differences in the slope of the catchment with the creek catchment being steeper than the spring catchment. Indeed, in the Andes-Amazon high b-values (close to zero) were found in

**Table 2**  
Summary of *b*-Values and  $CV_C/CV_Q$  Used for the Evaluation of Concentration—Discharge Relationships

	Major elements						Trace elements						Anion and dissolved organic compounds			
	Ca	K	Mg	Na	Si	S	Al	Ba	Cu	Fe	P	Sr	Zn	DOC	DON	Cl
Spring water (SW)																
b-value	−0.22	−0.01	−0.22	−0.08	0.02	−0.15	−0.19	−0.17	−0.06	−0.03	0.14	−0.18	−0.07	0.01	−0.10	−0.03
±SE	0.00	0.00	0.00	0.00	0.00	0.01	0.03	0.01	0.01	0.07	0.01	0.00	0.01	0.03	0.03	0.00
R <sup>2</sup>	0.90	0.01	0.90	0.62	0.15	0.34	0.22	0.80	0.07	0.00	0.29	0.87	0.12	0.00	0.03	0.20
p-value	<0.001	<0.5	<0.001	<0.001	<0.001	<0.001	<0.001	<0.001	<0.001	<1	<0.001	<0.001	<0.001	<1	<0.01	<0.001
$CV_C/CV_Q$	0.21	0.08	0.20	0.09	0.04	1.00	0.54	0.16	0.22	1.7	0.23	0.18	0.18	0.47	0.52	0.06
Creek water (CW)																
b-value	−0.19	−0.03	−0.14	−0.10	−0.01	−0.14	−0.06	−0.13	0.02	0.27	−0.17	−0.16	−0.08	0.06	0.00	−0.04
±SE	0.01	0.01	0.00	0.00	0.01	0.01	0.04	0.00	0.01	0.08	0.01	0.00	0.01	0.02	0.03	0.00
R <sup>2</sup>	0.79	0.08	0.73	0.59	0.01	0.39	0.02	0.83	0.01	0.10	0.51	0.80	0.12	0.02	0.00	0.23
p-value	<0.001	<0.001	<0.001	<0.001	<0.5	<0.001	<0.5	<0.001	<0.5	<0.01	<0.001	<0.001	<0.001	<0.01	<1	<0.001
$CV_C/CV_Q$	0.24	0.11	0.18	0.13	0.08	0.90	0.25	0.16	0.25	0.95	0.25	0.20	0.22	0.53	0.57	0.07

Note. SE: standard error of the mean; orange labeled numbers indicate statistical insignificance. Color coding: blue: dilution behavior (*b*-value < −0.1), green: chemostatic behavior (*b*-value between −0.1 and 0,  $CV_C/CV_Q \ll 1$ ), enrichment behavior (*b*-value > 0).

catchments with high slope and low *b*-values in catchments with low slope (Torres et al., 2015). As one potential explanation Torres et al. (2015) suggests a link between relief, erosion rate, soil residence time, and the degree of chemical alteration. More specifically, high relief results in high erosion rate (Montgomery et al., 2002), high erosion rate in turn results in low soil residence time, and low soil residence time results in weakly weathered regolith for a given fluid flow. Superimposed onto the fluid residence time model of Maher (2011) fluid residence time that depends on topography may both delay or accelerate the attainment of equilibrium. For example, high relief potentially increases the area of basins thereby extending the length of flow paths and in turn fluid residence time. In any case, fluids flowing through regolith with a high abundance of primary reactive minerals approach thermodynamic equilibrium faster than fluids flowing through highly weathered regolith, thereby showing chemostatic behavior.

## 5. Discussion

### 5.1. The Origin of Chemostasis

A first potential explanation for the chemostatic behavior of K, Na Si, Al, Cu, Fe, Zn, and Cl in the steep, first-order headwater catchment at the Conventwald is the drainage of atmospherically derived, chemically passive, hence conservatively behaving solutes in the watershed such as Cl. Given that annual input fluxes of Cl in bulk precipitation ( $Dep_{BP}^{Cl}$ , Equation 3, Figure 3) are similar to annual solute export fluxes of Cl in creek water ( $W_{CW}^{Cl}$ , Equation 8, Figure 3), Cl can indeed be considered to transit the Conventwald passively.

A second potential explanation of chemostasis is chemical equilibrium between the dissolution and formation of secondary solids. To assess this hypothesis, mineral saturation indices were calculated with PhreeqC (Figure 4). Saturation indices for primary minerals are negative, and hence, apart from quartz, indicate mineral dissolution. Saturation indices for secondary solids are positive, hence indicate neoformation. Clow and Drever (1996) and Clow and Mast (2010) suggested that chemostatic behavior occurs, when metastable amorphous or poorly crystalline minerals are formed at low discharge (e.g., baseflow) and are redissolved at high discharge as then their mineral saturation indices fall below zero. In our study, the mineral saturation index of halloysite fluctuates around zero in groundwater (Figure 4), when taking minimum and maximum pH values of pH 6 and pH 7 into account (c.f. Section 3.3.3), which is consistent with the chemostatic behavior of Al and Si. Likely, this finding also holds for the winter period, but due to the lack of Al measurements, saturation indices of halloysite could not be calculated for the winter period.

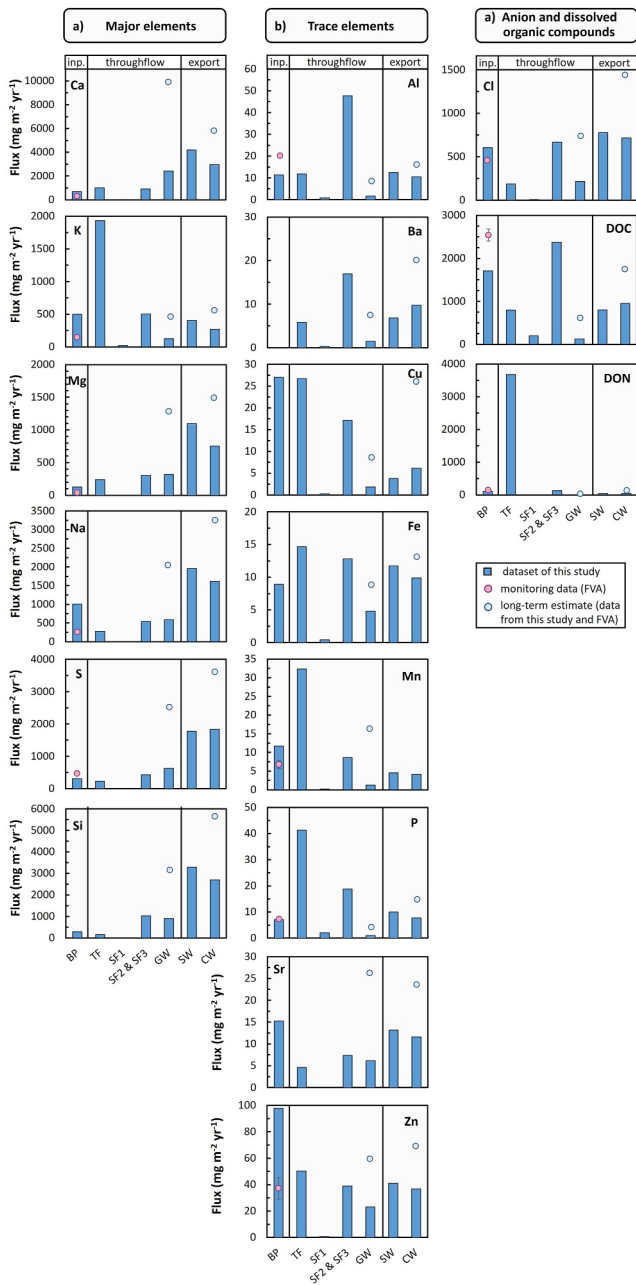


**Figure 3.** Solute fluxes of major elements (panel a), trace elements (panel b) and anion and dissolved organic compounds (panel c) in bulk precipitation (BP), throughfall (TF), subsurface flow SF1 (SF1: 0–30 cm) and subsurface flow SF2 and SF3 (SF2 and SF3: 30–320 cm), groundwater (GW), spring water (SW) and creek water (CW). The determination of solute fluxes is detailed in Section 3.4.1. Monitoring data cover the period from 1992 to 2019 and were sourced from the FVA. Long-term estimates of creek water were estimated by multiplying the long-term average of creek discharge (2004–2013, FVA) with solute concentrations as detailed in Section 3.4.1 (Equations 9 and 10).

A third explanation suggested for maintaining chemostatic behavior are ion exchange processes (e.g., Clow & Mast, 2010; Herndon et al., 2015), as demonstrated for Mg in the Susquehanna Shale Hills Critical Zone Observatory (SSHCZO, Pennsylvania, USA) (Bao et al., 2017) and in the Conventwald (Cai et al., 2022). This process is subject to several prerequisites: (a) sufficient exchangeable sites must be present, for example, in the form of organic carbon in the topsoil and charged mineral surfaces in the mineral soil and saprolite; (b) sufficient buffer capacity exists, which is the case if the exchangeable fraction is replenished after desorption; and (c) the permeability of soil and saprolite must be low so as to set a water residence time in soil and saprolite that allows the kinetics of ion exchange for desorption to run to completion. Prerequisite (a) is fulfilled because the Cambisol at the Conventwald contains exchangers of low to high cation exchange capacities, represented by an organic rich topsoil, and the clay minerals kaolinite, illite, smectite, chlorite, and vermiculite (X-ray diffraction analyses in Uhlig and von Blanckenburg (2019)). Prerequisite (b) can be evaluated by means of the turnover time of element X in the bioavailable fraction in soil—comprising mainly the exchangeable fraction but also the water-soluble fraction—with respect to an input flux into or output flux from the bioavailable soil compartment. Approaches to calculate these specific residence times were developed in Uhlig and von Blanckenburg (2019). The residence time of an element X in the bioavailable fraction in soil after release from primary minerals and before export into the stream is represented by the turnover time  $T_{\text{bioav}, W_{\text{stream}}}^X$  (Equation 13) that is calculated from the ratio of the inventory of the bioavailable fraction in soil ( $I_{\text{bioav}}^X$ , provided by Uhlig and von Blanckenburg (2019)) and the annual stream water export flux ( $W_{\text{stream}}^X$ ).

$$T_{\text{bioav}, W_{\text{stream}}}^X = \frac{I_{\text{bioav}}^X}{W_{\text{stream}}^X} \quad (13)$$

Vice versa, the period required to replenish the full inventory of the bioavailable fraction in soil by element supply through the chemical weathering flux ( $W_{\text{regolith}}^X$ , Equation 11) is represented by the turnover time  $T_{\text{bioav}, W_{\text{regolith}}}^X$  (Equation 14).

$$T_{\text{bioav}, W_{\text{regolith}}}^X = \frac{I_{\text{bioav}}^X}{W_{\text{regolith}}^X} \quad (14)$$

For most elements  $T_{\text{bioav}, W_{\text{stream}}}^X$  and  $T_{\text{bioav}, W_{\text{regolith}}}^X$  are similar (Table 3, Figure 5). Hence, elemental inventories are sufficiently large to cater for a large buffer pool. Consequently, prerequisite (b) is also fulfilled. However, due to the lack of measurements of water transit times through the weathering zone of the Conventwald, prerequisite (c) remains untestable at this stage. To address (c) we can explore relative element-specific ion exchange kinetics. A general rule of thumb dictates that the selectivity of a given cation for adsorption is lower for monovalent than for divalent cations. Consequently,  $\text{Mg}^{2+}$  and  $\text{Ca}^{2+}$  are more attracted by the solid phase than  $\text{Na}^+$  and  $\text{K}^+$ , hence also desorb slower. This explains the weak dilution behavior or, in other words, near-chemostatic behavior of Ca and Mg (Cai et al., 2022). The

chemostasis of K is consistent with sorption processes if it results from the seasonal transfer of interlayer K from and into the precursor minerals of illite, namely vermiculite and/or smectite. Both minerals were identified by X-ray diffraction analyses (Uhlig & von Blanckenburg, 2019). Illite formation was indeed found to be a reversible process that can be induced by plant–clay interactions (Barré & Velde, 2012).

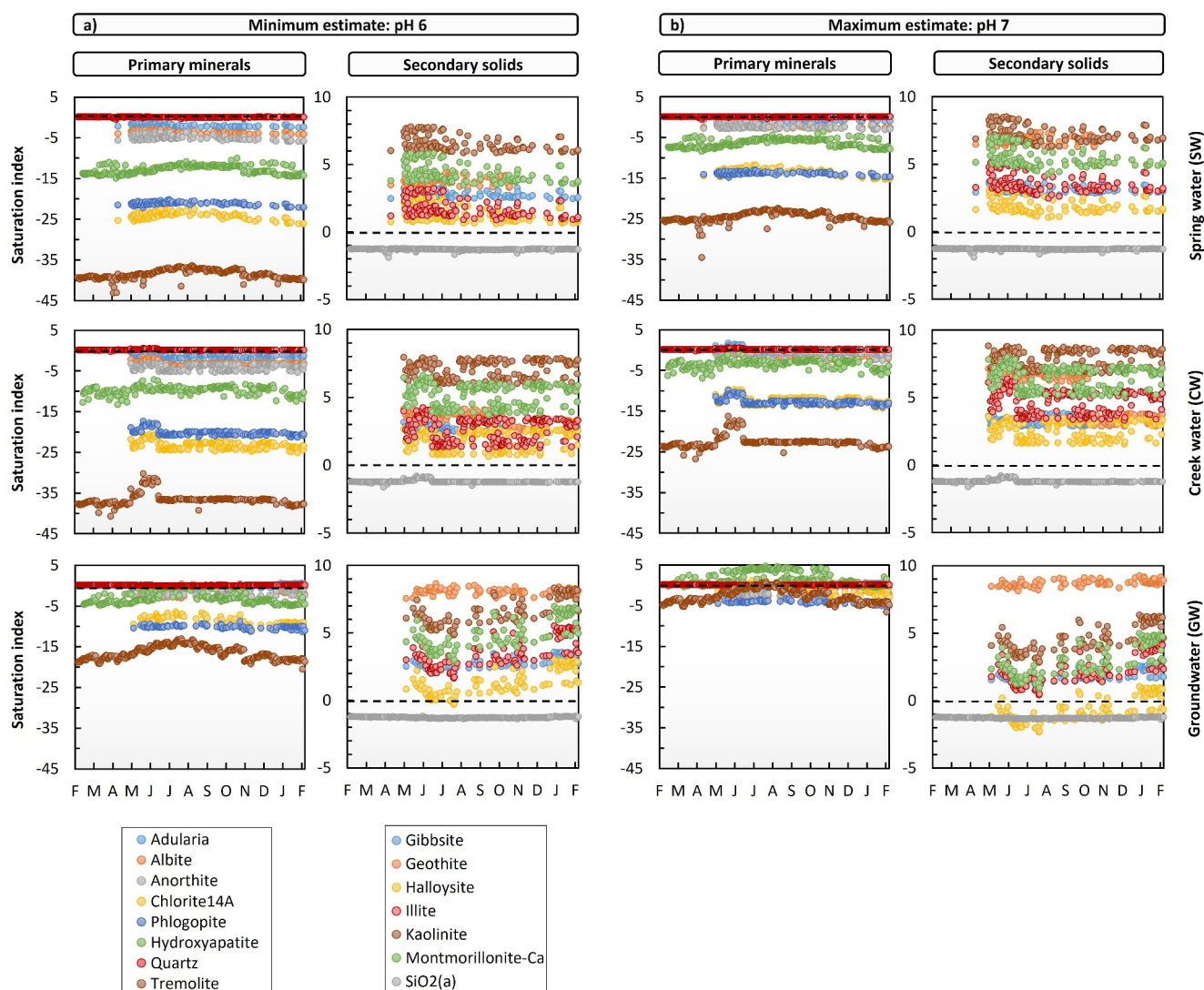


**Figure 4.** Seasonal variation of mineral saturation indices for primary minerals and secondary solids at minimum and maximum pH values (c.f. Section 3.3.3). Stippled lines indicate a saturation index of zero. Tremolite represents amphibole, adularia represents K-feldspar, and halloysite represents amorphous aluminosilicates. The data gap from March to April is due to the lack of Al measurements.

As a fourth explanation for chemostasis, we suggest flushing (Clow & Drever, 1996), that is the drainage of organic-derived solutes (e.g., DOC, DON, nutritive elements), colloids, and trace metals complexed with organic matter (e.g., Al, Cu, Fe, Mn, Zn) from the riparian zone into the stream (Herndon et al., 2015; Pacific et al., 2010; Trostle et al., 2016; Zhi et al., 2019). Given that subsurface flow (SF2 and SF3) contributes 90%–95% to the Conventwald’s creek discharge at high flow (EMMA), we identify subsurface flow as a source of flushing. However, flushing may be too weak to be manifested in positive C-Q slopes but strong enough to explain chemostatic behavior for the nutritive element K and the trace metals Al, Cu, Fe, Zn. Given that divalent and trivalent cations have a high affinity to form stable chelate structures, these trace metals are likely complexed with the functional groups of organic matter.

## 5.2. Implications for Short-Term Element-Specific Chemical Weathering Fluxes

As shown in Section 3.4.1 “short-term” element-specific chemical weathering fluxes ( $W_{\text{stream}}^X$ ) are calculated from the product of the concentration of element X in gauged stream water with the catchment area-normalized discharge and integrating this product over the entire sampling period (Equation 8, Equation 10). This practice

**Table 3**  
Inventories ( $I^X$ ), Turnover Times ( $T^X$ ) and Dissolved Export Efficiencies ( $DEE^X$ ) of Element X

	Major elements					Trace elements						
	Ca	K	Mg	Na	Si	Al	Ba	Fe	Mn	P	Sr	Zn
Inventories ( $\text{g m}^{-2}$ )												
$I_{\text{bioav}}^X$ 0–3 m <sup>a</sup>	220	81	85	22	n.d.	44	n.d.	2.6	35	82	n.d.	n.d.
$I_{\text{bioav}}^X$ 3–7 m <sup>a</sup>	2,600	190	780	50	n.d.	10	n.d.	7.4	13	100	n.d.	n.d.
Turnover times –0–7 m (yr)												
$T_{\text{bioav},W_{\text{CW}}}^X$ 0	672	666	788	37	n.d.	4,313	n.d.	853	n.d.	18,068	n.d.	n.d.
$T_{\text{bioav},W_{\text{SW}}}^X$	952	997	1,152	45	n.d.	5,140	n.d.	1,010	n.d.	23,537	n.d.	n.d.
$T_{\text{bioav},W_{\text{regolith}}}^X$	513	271	433	30	n.d.	7.6	n.d.	2.2	n.d.	2,167	n.d.	n.d.
Dissolved export efficiencies (dimensionless)												
* $DEE_{\text{regolith}}^X$	0.97	0.43	0.70	1.2	0.31	0.00	0.34	0.00	n.d.	0.15	0.36	1.7
* $DEE_{\text{regolith,Na}}^X$	0.85	0.38	0.61	1.0	0.27	0.00	0.27	0.00	n.d.	0.13	0.31	1.5
* $DEE_{\text{saprolite}}^X$	2.5	0.41	1.1	0.70	0.18	0.00	0.13	0.00	0.19	0.04	0.38	1.5
* $DEE_{\text{saprolite,Na}}^X$	3.6	0.59	1.5	1.0	0.26	0.00	0.17	0.00	0.28	0.06	0.54	2.2

Note. n.d.: not determined; SE: standard error of the mean. <sup>a</sup>Data of bioavailable fraction from Uhlig and von Blanckenburg (2019). Bioavailable fraction represents the water-soluble fraction (mQ-H<sub>2</sub>O, 18 MΩ, pH 5, 24h extraction duration) and the easily exchangeable fraction (1M NH<sub>4</sub>OAc, neutral pH, 2h extraction duration) for all elements except P. The bioavailable fraction of P refers to the inorganic products (P<sub>i</sub>) of the Hedley sequential P fractionation method, namely resin-P, HCO<sub>3</sub>-P<sub>i</sub>, and 1M HCl- P<sub>i</sub>. <3 m denotes the average concentration within the upper 3 m of regolith and >3 m denotes the average concentration between 3 m and the base of saprolite at 7 m depth.

only results in representative chemical weathering fluxes if several prerequisites are met. Prerequisites include (a) atmospheric inputs are negligible or can be corrected for; (b) fluxes of secondary mineral formation and dissolution, adsorption and desorption, and nutrient uptake and organic matter decomposition are balanced in non-logged forests of stable climax (final stage of ecosystem succession), for example, no net retention or release of element X from or into the Critical Zone compartments is involved; (c) stream water captures the entirety of the catchment's water export, for example, groundwater export is negligible; and (d) the sampling period covers the whole range of potential rainfall intensities and hence discharge variation with time. Whereas prerequisite (a) to (c) can be tested by sophisticated sampling of the Critical Zone, rainfall and discharge underlie stochastic events (e.g., Botter et al., 2007; Vallejo-Bernal et al., 2021), meaning that the time period of a few decades over which gauging programs are running is likely too short to record the entirety of discharge including the potential flood with a centennial recurrence interval. Considering C-Q relationships presented and discussed in the preceding sections, short-term element-specific weathering fluxes can only be considered to be representative in cases of perfect dilution behavior, meaning the b-value equals minus one. Only in this case are solute concentrations perfectly correlated with stream discharge. Hence, any missing C-Q pair, resulting from unrecorded discharge events, would not bias short-term chemical weathering fluxes. In contrast, if b-values are larger than minus one—indicating either weak dilution, chemostatic or even enrichment behavior—and if any high discharge event remained unrecorded,  $W_{\text{stream}}^X$  would inevitably be underestimated. For example,  $W_{\text{stream}}^X$  would be underestimated by about 7%, if a flood of the century, discharging about one third of annual discharge, would be missing in, for example, a 20-year gauging period. If the flood of the century would also shift the C-Q relationship from chemostatic behavior (e.g., b-value = 0) to enrichment behavior (e.g., b-value = 0.5), because preceding flushing events were too weak to cause enrichment behavior, then colloids will only be mobilized and transported in this one flood event and  $W_{\text{stream}}^X$  would have been underestimated by about 80%.

For the timescale of regolith turnover (“long-term”), element-specific chemical weathering fluxes can be determined from solids. Specifically, mass transfer and cosmogenic nuclide-derived element-specific chemical weathering fluxes ( $W_{\text{regolith}}^X$ ) integrate over  $10^3$ – $10^5$  years, hence over such long timescales that  $W_{\text{regolith}}^X$  can be considered to be governed by a deterministic climate state (Wilkinson, 2015). In other words, element loss throughout the whole weathering zone features the complete net release of elements through chemical weathering. Thus, comparing  $W_{\text{regolith}}^X$  with  $W_{\text{stream}}^X$  allows to assess whether the gauging period captures the entirety of

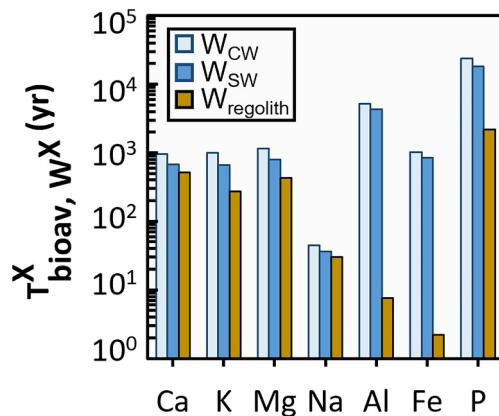


**Figure 5.** Turnover times of element X in the bioavailable fraction in soil with respect to the solute export flux of the creek ( $W_{CW}^X$ ), the spring ( $W_{SW}^X$ ), or the chemical weathering flux ( $W_{regolith}^X$ ). The inventory of the bioavailable fraction in soil (Table 1 in Uhlig and von Blanckenburg (2019)) integrates over the entire soil-saprolite depth profile (0–7 m) and comprises the sum of the water-soluble fraction (mQ-H<sub>2</sub>O, 18M $\Omega$ , 24h) and the easily exchangeable fraction (1M NH<sub>4</sub>OAc, 2h) for all elements except P. Phosphorus comprises the inorganic products (P<sub>i</sub>) of the Hedley sequential fractionation method, namely resin-P<sub>i</sub>, HCO<sub>3</sub>-P<sub>i</sub>, and 1M HCl-P<sub>i</sub>.

sampled Critical Zone compartment or flux (von Blanckenburg et al., 2021). Colloids forming as secondary precipitates, for example, are mobilized and transported through soil macropores and rock fractures (Lægdsmand et al., 1999; Zhang et al., 2015) and might only arrive in the stream during high flow conditions, thus through flushing events (von Blanckenburg et al., 2021). The  $DEE_{regolith}^X$  can also be larger than unity if atmospheric inputs are underestimated.

$$DEE_{regolith}^X = \frac{W_{stream}^X}{W_{regolith}^X} \quad (15)$$

$$*DEE_{regolith}^X = \frac{W_{stream}^X}{W_{regolith}^X + Dep_{wet}^X + Dep_{dry}^X} \quad (16)$$

We can calculate the dissolved export efficiency at the Conventwald by forming the ratio of the short-term element-specific chemical weathering flux from the creek catchment (for  $W_{stream}^X$  we used  $*W_{CW}^X$  (Equation 9, Table 4, Figure 6) in Equation 16) over the long-term estimate of the element-specific chemical weathering flux ( $W_{regolith}^X$ , Equation 11, Table 4, Figure 6). The latter includes atmospheric wet deposition (for  $Dep_{wet}^X$  we used  $*Dep_{BP}^X$  (Equation 3, Table 4) in Equation 16) and, assuming complete dissolution, the dissolved flux of atmospheric dry deposition ( $Dep_{dry(max)}^X$ , Equation 4, Table 4). The  $*DEE_{regolith}^X$  (Table 3, Figure 7) amounts for major elements to values of 0.31 (Si), 0.43 (K), 0.70 (Mg), 0.97 (Ca), 1.2 (Na), and for trace elements to values of 0.00 (Al, Fe), 0.15 (P), 0.34 (Ba), 0.36 (Sr), and 1.7 (Zn). The  $*DEE_{regolith}^{Zn}$  is substantially larger than one, suggesting insufficient consideration of atmospheric input fluxes that are more than twice as high in bulk precipitation than in the creek's solute export flux (Table 4, Figure 3). It is striking that the  $*DEE_{regolith}^X$  is zero for Fe, the element with the strongest enrichment behavior (b-value = 0.27). It is also clear that the  $*DEE_{regolith}^X$  is low (e.g.,  $0 \leq DEE_{regolith}^X < 0.4$ ) for elements like Al, Mn, P, and Si that are either main components of colloids (Trostle et al., 2016) or minor components in colloids (Aguirre et al., 2017; Gottselig et al., 2020; Mills et al., 2017; Moravec et al., 2021). Thus, an explanation for the deficits of Al, Fe, and a fraction of Si is its presence in natural nanoparticles (1–100 nm) or fine colloids (100–300 nm) that formed secondary in the weathering zone and remained undetected in this study. This lack of detection can be either due to i) particle loss occurring during water filtration, or (b) its escape from the regolith at high flow conditions, which were missed during our sampling period (cause iii or iv above).

dissolved element export from the watershed, or, whether low frequency high discharge events, such as the flood of the century, are missing in  $W_{stream}^X$ . This comparison has been quantified by the “Dissolved Export Efficiency” ( $DEE_{regolith}^X$ ) metric (von Blanckenburg et al., 2021; Schuessler et al., 2018; Uhlig et al., 2017).

### 5.3. Dissolved Export Efficiency in Regolith

The dissolved export efficiency ( $DEE_{regolith}^X$ , Equation 15) quantifies the proportion of element X released by chemical weathering in regolith ( $W_{regolith}^X$ ) that arrives in the stream dissolved load ( $W_{stream}^X$ ). In settings, in which inputs of atmospheric wet deposition such as rainwater ( $Dep_{wet}^X$ ) and/or the dissolved fraction of dry deposition such as dust ( $Dep_{dry}^X$ ) are significant, the  $DEE_{regolith}^X$  requires taking atmospheric inputs into account, indicated by the asterisk in Equation 16 ( $*DEE_{regolith}^X$ ). Deficits in the stream dissolved load ( $0 \leq DEE_{regolith}^X < 1$ ) can be attributed to (a) an incomplete record of discharge variation with time; (b) the partitioning of nutrients into re-growing biomass or export of plant debris (Uhlig et al., 2017); (c) in-stream processes such as the formation and locking-away of micrometer-sized clay minerals or amorphous and crystalline oxides in stream water, or sediment-water cation exchange in the stream (Tipper et al., 2021); and/or (d) the presence of an un-

**Table 4**  
Annual Solute Fluxes in Water Compartments Sampled in This Study, and Millennial-Scale Chemical Weathering Fluxes

	Major elements						Trace elements								Anion and organic dissolved compounds			Water Flux ( $l\ m^{-2}\ yr^d$ )
	Ca	K	Mg	Na	Si	S	Al	Ba	Cu	Fe	Mn	P	Sr	Zn	DOC	DON	Cl	
	(mg m <sup>-2</sup> yr <sup>-1</sup> )						(mg m <sup>-2</sup> yr <sup>-1</sup> )								(mg m <sup>-2</sup> yr <sup>-1</sup> )			
Flux estimates (data set of this study)																		
Dep <sub>BP</sub> <sup>X</sup>																		
Flux	691	498	129	1,008	298	306	11	n.d.	27	8.9	12	7.1	15	98	1,710	109	606	1,135
uncertainty	142	69	106 <sup>b</sup>	13	155 <sup>b</sup>	93 <sup>b</sup>	31	1.1	n.d.	2.7	0.89	2.5 <sup>b</sup>	0.71		9.8	142	11	85
Dep <sub>TF</sub> <sup>X</sup>																		
Flux	1,003	1,933	240	280	162	235	12	5.8	27	15	32	41	4.6	50	800	3,682	187	759
uncertainty	100	193	24	28	16	23	1.2	0.58	2.7	1.5	3.2	4.1	0.69 <sup>b</sup>	5.0	78	339	26	
W <sub>SF1</sub> <sup>X</sup>																		
Flux	25	23	4.8	2.5	8.5	2.8	0.84	0.31	0.29	0.41	0.16	2.0	0.11	0.72	199	7.0	7.7	3.6
uncertainty	3.3 <sup>b</sup>	2.1 <sup>b</sup>	0.64 <sup>b</sup>	0.14 <sup>b</sup>	0.93 <sup>b</sup>	0.31 <sup>b</sup>	0.09 <sup>b</sup>	0.04 <sup>b</sup>	0.03 <sup>b</sup>	0.04 <sup>b</sup>	0.04 <sup>b</sup>	0.34 <sup>b</sup>	0.01 <sup>b</sup>	0.08 <sup>b</sup>	24 <sup>b</sup>	0.93 <sup>b</sup>	0.81 <sup>b</sup>	
W <sub>SF2+SF3</sub> <sup>X</sup>																		
Flux	930	504	302	539	1,035	434	48	17	17	13	8.7	19	7.4	39	2,377	134	669	405
uncertainty	184 <sup>b</sup>	104 <sup>b</sup>	50 <sup>b</sup>	165 <sup>b</sup>	117 <sup>b</sup>	112 <sup>b</sup>	13 <sup>b</sup>	3.7 <sup>b</sup>	2.2 <sup>b</sup>	4.0 <sup>b</sup>	2.6 <sup>b</sup>	6.1 <sup>b</sup>	1.4 <sup>b</sup>	6.6 <sup>b</sup>	549 <sup>b</sup>	29 <sup>b</sup>	59 <sup>b</sup>	
W <sub>GW</sub> <sup>X</sup>																		
Flux	2,428	126	320	587	901	632	1.8	1.5	1.9	4.8	1.3	0.94	6.1	23	126	7	218	171
uncertainty	243	13	32	59	90	63	0.18	0.15	0.19	0.49 <sup>b</sup>	0.31 <sup>b</sup>	0.09	0.61	2.3	13	1	22	
W <sub>SW</sub> <sup>X</sup>																		
Flux	4,195	407	1,098	1,964	3,299	1,778	13	6.8	3.8	12	4.6	10	13	41	803	40	780	613
uncertainty	419	41	110	196	330	178	1.3	0.68	0.38	1.2	0.46	1.0	1.3	4.1	80	4	78	
W <sub>CW</sub> <sup>X</sup>																		
Flux	2,962	272	751	1,616	2,703	1,840	11	9.7	6.2	9.9	4.2	7.7	12	37	952	45	717	609
uncertainty	296	27	75	162	270	184	0.69 <sup>b</sup>	1.0	0.6	1.1 <sup>b</sup>	0.32 <sup>b</sup>	0.77	1.2	3.7	95	5	72	
Flux estimates (based on monitoring data) <sup>a</sup>																		
Dep <sub>BP</sub> <sup>X c</sup>																		
Flux	361	141	51	281	n.r.	472	20	n.r.	n.r.	n.r.	6.8	7.5	n.r.	37	2,543	139	453	
uncertainty	16	11	2.0	16	n.r.	45	0.74	n.r.	n.r.	n.r.	1.1	0.96	n.r.	8.2	140	15	23	
Flux estimates (based on modeled mass fluxes and UCC concentrations) <sup>d</sup>																		
Dep <sub>dust</sub> <sup>X</sup>																		
Min	60	56	27	58	616	n.r.	161	1.1	0.05	70	1.2	0.70	0.14		n.r.	n.r.	n.r.	
Max	150	140	67	145	1,540	n.r.	402	2.8	0.13	175	3.0	1.8	0.36		n.r.	n.r.	n.r.	
Flux estimates (based on monitoring data and the data set of this study) <sup>e</sup>																		
W <sub>GW</sub> <sup>X c</sup>																		
Flux	9,960	457	1,281	2,073	3,113	2,505	9.11	7.6	8.5	8.8	16	4	26	60	626	40	740	569
W <sub>CW</sub> <sup>X c</sup>																		
Flux	5,801	559	1,496	3,223	5,602	3,617	16	20	26	13	n.d.	15	24	69	1,771	126	1,445	1,265



**Table 4**  
Continued

	Major elements						Trace elements								Anion and organic dissolved compounds			Water Flux
	Ca	K	Mg	Na	Si	S	Al	Ba	Cu	Fe	Mn	P	Sr	Zn	DOC	DON	Cl	(l m <sup>-2</sup> yr <sup>a</sup> )
	(mg m <sup>-2</sup> yr <sup>-1</sup> )						(mg m <sup>-2</sup> yr <sup>-1</sup> )								(mg m <sup>-2</sup> yr <sup>-1</sup> )			
Flux estimates (based on a published data set) <sup>f</sup>																		
W <sub>saprolite</sub> <sup>X</sup>																		
Flux	3,460	825	1,089	2,530	15,263	n.d.	6,006	55	n.d.	2,654	74	89	53	2				
W <sub>regolith</sub> <sup>X</sup>																		
Flux	5,447	1,006	2,025	2,386	16,200	n.d.	7,104	57	n.d.	4,467	80	83	49	2				

Note. n.r.: not reported, n.d.: not determined; Uncertainties were estimated to be 10% unless otherwise stated. <sup>a</sup>Average value of monitoring data (1992–2019) sourced from the FVA. <sup>b</sup>Uncertainty estimated by error propagation of the standard error from average annual concentration data. <sup>c</sup>Long-term estimates of fluxes. <sup>d</sup>Detailed in Section 3.4.1 and calculated from Equation 4. <sup>e</sup>Calculated using C-Q relationships of creek water, the long-term average of discharge (2004–2013) and the contribution of groundwater (45%) to discharge taken from the EMMA. <sup>f</sup>W<sub>regolith</sub><sup>X</sup> is sourced from Uhlig and von Blanckenburg (2019) and W<sub>saprolite</sub><sup>X</sup> was calculated from Equation 12 as detailed in Section 3.4.2.

With respect to possibility (a) about 150 ml of all water samples of this study were passed through a polyethersulfone (PES) filter of 0.8 μm pore size prior to analysis. Although this pore size is larger than the size of natural nanoparticles and fine colloids, we believe that they might be retained within the complicated and multi-layered structure of the cellulose filter membrane while passing through the ~10<sup>2</sup> μm thick filter, which is about 10<sup>2</sup> to up to 10<sup>4</sup> times thicker than the size of natural nanoparticles and fine colloids. Such particle retention was found by Zirkler et al. (2012) and termed “loss on filtration.”

Possibility (b) entails export of natural nanoparticles and fine colloids during periods of high flow, which were formed secondary and stored upon export during periods of low flow in soil macropores or rock fractures that remained unsampled in this study. Evidence for this hypothesis is provided in the form of positive C-Q relationships for likely colloidal-influenced elements such as Al, Fe, and Mn (Aguirre et al., 2017; Herndon et al., 2015; Hoagland et al., 2017; Trostle et al., 2016). These colloids have been hypothesized to be preferentially exported during flushing events, where a rising water table taps into shallow soil (Zhi et al., 2019), meaning that the hydrologic connectivity between shallow soil and the stream becomes re-established. This re-establishment allows inorganic colloids, which may be complexed with dissolved organic matter, to be mobilized and eventually transported into the stream. The deficits of Al and Fe found in creek water might have arisen if large flushing events have not been included in this study's gauging period. For example, high flow conditions might have been insufficient to trigger a flushing event that mobilized colloids, or the automatic sampling, taking place once every 24 hr, may have missed such an event. This interpretation suggests that the b-value of Al and Fe, and perhaps of Si too, should be much more positive than found in this study. For example, b-values of Al and Fe are consistently more positive in the watersheds of Marshall Gulch (Arizona, USA; Al: ~0.75, Fe: ~0.65, Trostle et al. (2016)), Garner Run (Pennsylvania, USA; Al: 0.21, Fe: 0.68, Hoagland et al. (2017)) and Upper Hafren (Plynlimon, Wales; Al: 0.58, Fe: 0.33, Herndon et al. (2015)) than in our Conventwald creek watershed (Al: -0.06, Fe: 0.27). However, given the wide range of locations, this consistency may also be due to different catchment characteristics. We return to the discussion of colloids below and continue with the deficits found in creek water for the remaining elements, among which K, Ca, Mg, and P are plant essential.

We attribute deficits found for K, Ca, Mg and P in creek water to nutrient uptake by forest trees followed by storage in re-growing biomass and natural export in biogenic particulate form such as coarse woody debris, leaf litter, or fine-grained degraded biomass. Given that the Conventwald is a protected forest since the 1970's, element export through the removal of timber harvest can be excluded. By two lines of evidence this explanation is also applicable to the deficits found for the non-plant essential elements Ba and Sr (Marschner, 2011). First, Ba and Sr are commonly present at the μg g<sup>-1</sup> level in plants (Kabata-Pendias, 2011). Second, the export of Ba and Sr in particulate organic matter was shown to be a likely explanation based on metal stable isotopes that fractionate only via plant uptake if those elements are not returned to soil. This effect was demonstrated by Charbonnier et al. (2020, 2022) for Ba stable isotopes in the Amazon rainforest, Oeser and von Blanckenburg (2020) for Sr

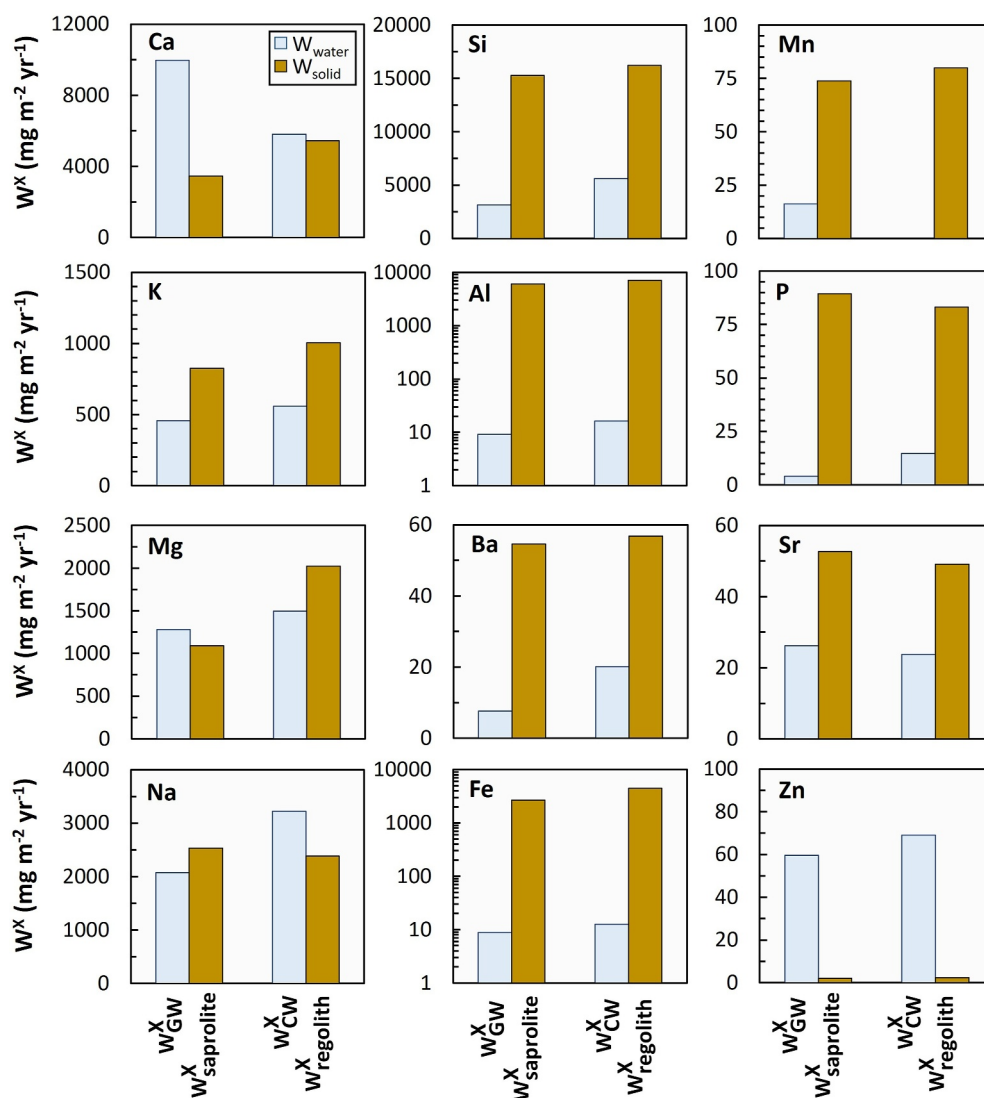


**Figure 6.** Fluxes of element X dissolved in water from groundwater ( $W_{\text{GW}}^{\text{X}}$ ) and creek water ( $W_{\text{CW}}^{\text{X}}$ ), integrating over annual timescales (in blue), and their release fluxes by weathering in saprolite ( $W_{\text{saprolite}}^{\text{X}}$ ) and the entire weathering zone ( $W_{\text{regolith}}^{\text{X}}$ ), integrating over several millennia (in brown). To minimize year-to-year variations in bulk precipitation in the dissolved fluxes in saprolite and the creek, the respective fluxes were calculated from C-Q relationships shown for the creek in Figure S1 in Supporting Information S1. In doing so, long-term discharge (2004–2013) and the contribution of groundwater (45%) and subsurface flow (51%) to discharge taken from the EMMA were used.

stable isotopes along a climate and vegetation gradient at the coastal mountains of Chile, and Bouchez and von Blanckenburg (2021) for watershed along a global transect of mountain landscapes that differ in erosion rates called an “erodosequence” (von Blanckenburg et al., 2021). Moreover, even though Si is only a plant-beneficial element but a main constituent of secondary solids, Frings et al. (2021) found that a surprising large amount of up to 39% of Si solubilized from primary minerals is exported in biogenic particulate form such as phytoliths contained in plant litter or coarse woody debris, or in-stream produced biogenic silica, explaining about half of the deficit found in our study.

Finally, in-stream processes such as (a) sediment-water cation exchange and (b) secondary mineral formation can be regarded unlikely in explaining deficits in the stream dissolved load. Regarding (a) sediment-water cation exchange is unlikely because, unlike stream water entering the ocean, there is no major change in the water composition when soil water or groundwater enter the stream. Regarding (b) saturation indices of secondary solids are positive in both groundwater entering the stream, and in stream water. Thus, secondary solids, be it

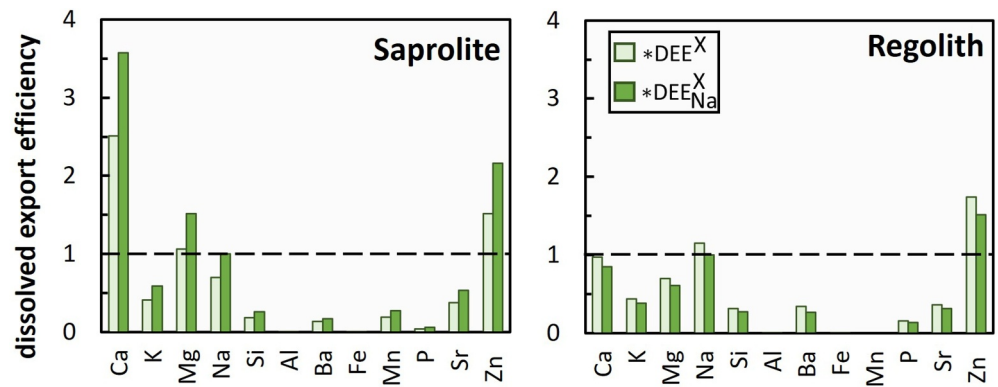


**Figure 7.** Dissolved export efficiency from measured fluxes ( $*DEE^X$ ) and from Na-normalized fluxes ( $*DEE^X_{Na}$ ) for saprolite and regolith (\* indicates that the DEE takes atmospheric deposition fluxes into account). The dashed line denotes the dissolved export efficiency of unity, indicating balanced fluxes. Elemental fluxes in water from the depth of saprolite ( $W^X_{GW}$ ) and creek ( $W^X_{CW}$ ) were determined from C-Q relationships and mean discharge from 2004 to 2013 (provided by courtesy of FVA) except for Mn (where the data set for Mn concentrations was limited). For Mn we thus followed the approach from Equation 7 and Equation 8.

nanometer-sized colloids or micrometer-sized secondary minerals, amorphous oxides or crystalline oxides, are most likely formed and stored in the groundwater aquifer and eventually flushed into, but not formed in the stream.

#### 5.4. Na-Normalized Dissolved Export Efficiency in Regolith

Returning to the incomplete record of stochastic rainfall events or discharge variations on the  $10^1$  to  $10^2$  time-scales, a potential bias may arise in solute export relative to the  $10^3$ – $10^5$  timescale over which discharge can be considered to be deterministic with respect to climate and weathering. Such potential bias can be catered for by normalizing the fluxes of  $W^X_{regolith}$  and  $W^X_{stream}$  over its respective fluxes of a conservatively behaving element like Na ( $DEE^X_{Na,regolith}$  in Equation 17 (Uhlig et al., 2017)). Including atmospheric input yields  $*DEE^X_{Na,regolith}$  (Equation 18, Schuessler et al. (2018)). Sodium is considered to be conservative because it is neither incorporated into secondary solids nor utilized by forest trees in significant quantities.

$$DEE^X_{Na,regolith} = \frac{\frac{W^X_{stream}}{W^X_{regolith}}}{\frac{W^X_{stream}}{W^X_{regolith}}} \quad (17)$$

$$*DEE^X_{Na,regolith} = \frac{\frac{W^X_{stream}}{W^X_{regolith}}}{\frac{W^X_{regolith}}{W^X_{regolith}} + \frac{Dep^X_{wet}}{W^X_{regolith}} + \frac{Dep^X_{dry}}{W^X_{regolith}}} \quad (18)$$

Values of the  $*DEE^X_{Na,regolith}$  (Table 4, Figure 7) are slightly lower than their non-Na normalized values and amount for major elements to 0.27 (Si), 0.38 (K), 0.61 (Mg), 0.85 (Ca), and for trace elements to 0.00 (Al, Fe), 0.13 (P), 0.27 (Ba), 0.31 (Sr), and 1.5 (Zn). In principle, deficits found in the creek's solute export flux can still be explained by retention in re-growing forest biomass, export in biogenic particulate from and colloidal export.

However, even though the Na-normalization cancels out the amount of discharge, the Na-normalization of the  $DEE^X_{Na,regolith}$  might introduce a bias. On the one hand, this bias may be introduced if ecosystem succession changes the type of ecosystem from woodland to grassland during the gauging period, because unlike trees, grasses take up Na as a nutrient. On the other hand, a bias may be introduced if Na does not show perfect dilution behavior, meaning that the b-value for Na deviates from minus one as is the case in the majority of watersheds

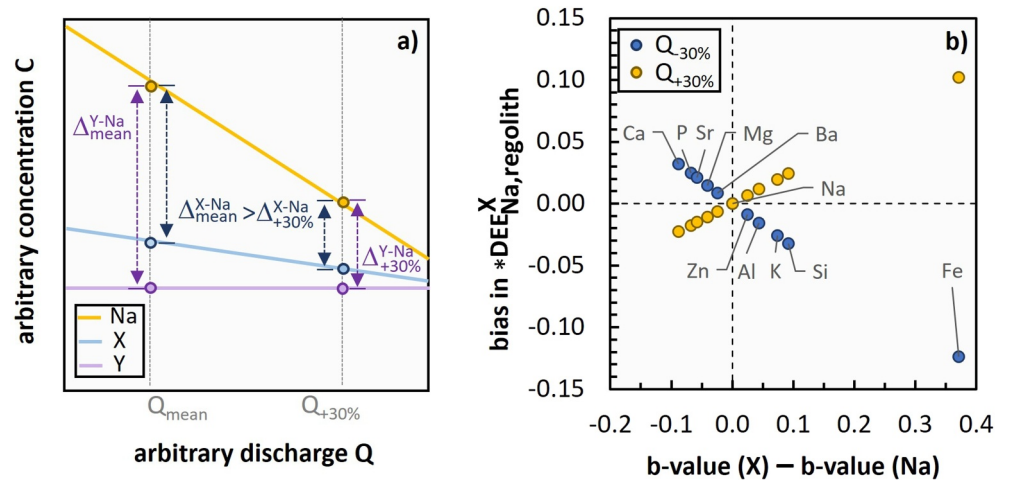


**Figure 8.** Graphical representation of the effect of the difference in b-values of a given element X and Na, respectively, on the Na-normalized “dissolved export efficiency” ( $DEE^X_{Na,regolith}$ ), under variable discharge. Panel (a) conceptually illustrates concentration (C)—discharge (Q) relationships for elements with contrasting C-Q slopes (b-values) with dilution behavior (Na), weak dilution behavior (element X), and chemostatic behavior (element Y). Circles illustrate two hypothetical C-Q settings at mean discharge ( $Q_{mean}$ ) and at a 30% higher discharge ( $Q_{+30\%}$ ). The concentration difference between an element and Na (e.g.,  $\Delta X-Na$ ) at  $Q_{mean}$  and  $Q_{+30\%}$ , respectively, depends on the b-value of the given element. Panel (b) illustrates a potentially introduced bias in the dissolved export efficiency  $*DEE^X_{Na,regolith}$ . Discharge was varied by 30% around this studies' creek mean value from 2004–2013 and represents the maximum value of the precipitation anomaly found in Germany from 1881 to 2022 with reference period from 1961 to 1990 (Deutscher Wetterdienst, 2021). b-values were taken from C-Q fits shown in Figure S1 in Supporting Information S1. The X-axis shows the difference between the b-value of a given element X (or Na) and that of Na. The bias in  $DEE^X_{Na,regolith}$  introduced by the Na normalization is negligible for almost all elements.

(see, for example, Godsey et al. (2009) for US catchments). Possibility (a) can be ruled out in the Conventwald due to field observation over the gauging period. Possibility (b) was tested by estimating the potential bias using C-Q fits from the creek (Figure S1 in Supporting Information S1), whilst varying creek discharge by  $\pm 30\%$  around the mean value from 2004–2013. The 30% discharge variation represents the maximum value of the rainfall anomaly found in Germany from 1881–2022 to the reference period 1961–1990 (Deutscher Wetterdienst, 2021). Note that 30% is also the deviation of early Holocene rainfall to modern-day rainfall in global river catchments (Aerts et al., 2006). We assessed how these maximum shifts in discharge translate into a potential bias in  $*DEE^X_{Na,regolith}$ . Such bias might arise if b-values of element X differ to varying degrees from that of Na (Figure 8). At the Conventwald, 30% discharge variation would bias the  $*DEE^X_{Na,regolith}$  by only  $\pm 0.01$  to  $\pm 0.03$  for all elements but Fe, because the elements show either chemostatic behavior, as does Na, or only weak dilution behavior (near chemostatic behavior like Ca and Mg). The bias is largest for Fe ( $\pm 0.12$ ), which is an enrichment-behaving element whereas Na behaves chemostatic. As the bias introduced into the  $DEE^X_{Na,regolith}$  is minor and overall patterns between elements are not affected, we conclude the Na-normalized  $DEE^X_{Na,regolith}$  to represent a valid estimate that accurately eliminates differences in discharge.

### 5.5. The Depth of Stream Deficit Generation

Critical Zone research increasingly emphasizes the importance of the deep Critical Zone in ecosystem functioning (e.g., Dawson et al., 2020; McCormick et al., 2021; Rempe & Dietrich, 2018; Tune et al., 2020; Uhlig et al., 2020). The sampling strategy of this study allows to localize the depth at which deficits in the stream dissolved export flux are generated. To this end, the long-term element-specific chemical weathering flux was calculated separately from the whole weathering profile to the saprolite located below three m ( $W^X_{saprolite}$ , Equation 12). To estimate the dissolved export efficiency for the saprolite at 3–7 m depth ( $DEE^X_{Na,saprolite}$ ), the solute flux of groundwater was used. We argue groundwater to be suitable because the groundwater table fluctuates around the interface of saprolite and weathered bedrock at 7 m depth. Thus, the Na-normalized fluxes of  $W^X_{groundwater}$  (for

$W_{\text{groundwater}}^X$  we used  $*W_{\text{GW}}^X$ , Equation 9, Table 3) were ratioed over the Na-normalized fluxes of  $W_{\text{saprolite}}^X$  in Equation 19. The latter included atmospheric wet deposition (for  $\text{Dep}_{\text{wet}}^X$  we used  $*\text{Dep}_{\text{BP}}^X$  (Equation 3, Table 4) in Equation 20) and, assuming complete dissolution, the dissolved flux of atmospheric dry deposition ( $\text{Dep}_{\text{dry(max)}}^X$ , Equation 4, Table 4) in Equation 20 ( $*\text{DEE}_{\text{Na,saprolite}}^X$ ).  $\text{DEE}_{\text{Na,saprolite}}^X$  must be viewed as an approximate estimate only, as annual solute loss beneath the groundwater well sampling depth of 7 m is not accounted for.

$$\text{DEE}_{\text{Na,saprolite}}^X = \frac{\frac{W_{\text{groundwater}}^X}{W_{\text{groundwater}}^{\text{Na}}}}{\frac{W_{\text{saprolite}}^X}{W_{\text{saprolite}}^{\text{Na}}}} \quad (19)$$

$$*\text{DEE}_{\text{Na,saprolite}}^X = \frac{\frac{W_{\text{groundwater}}^X}{W_{\text{groundwater}}^{\text{Na}}}}{\frac{W_{\text{saprolite}}^X + \text{Dep}_{\text{wet}}^X + \text{Dep}_{\text{dry}}^X}{W_{\text{saprolite}}^{\text{Na}} + \text{Dep}_{\text{wet}}^{\text{Na}} + \text{Dep}_{\text{dry}}^{\text{Na}}}} \quad (20)$$

Deficits in the dissolved load are found for almost all elements in the saprolite. Only for Ca, Mg and Zn the  $*\text{DEE}_{\text{Na,saprolite}}^X$  exceeds unity. The high  $*\text{DEE}_{\text{Na,saprolite}}^X$  for Zn may be attributed to an erroneous estimate for atmospheric inputs. In this regard we note that atmospheric input fluxes of Zn ( $\text{Dep}_{\text{BP}}^{\text{Zn}}$ , Table 4) are more than twice as high than solute export fluxes of Zn ( $W_{\text{CW}}^{\text{Zn}}$ , Table 4, Figure 3). The  $*\text{DEE}_{\text{Na,saprolite}}^X > 1$  of Ca and Mg is most likely related to a methodological artifact. This artifact arises as hornblende dissolution is fully represented in  $W_{\text{GW}}^X$  but only partly in  $W_{\text{saprolite}}^X$ . This is because weathered bedrock was used as starting material for  $W_{\text{saprolite}}^X$ , meaning  $W_{\text{saprolite}}^X$  only accounts for the loss of Ca and Mg occurring during the formation of saprolite from weathered bedrock. This calculation, however, fails to include the fraction of Ca and Mg that was lost during the formation of weathered bedrock from unweathered parent bedrock, which shows up in  $W_{\text{GW}}^X$ . Evidence for preferential hornblende dissolution was provided by means of Mg stable isotopes (Cai et al., 2022), and X-ray diffraction analyses (Uhlig & von Blanckenburg, 2019). Preferential mineral dissolution running to completion at the base of the saprolite does not affect the other elements because the dissolution of rock-forming minerals other than hornblende mainly occurs during the formation of saprolite from weathered bedrock.

$*\text{DEE}_{\text{Na,saprolite}}^X$  is about zero for Al, Fe and P, and amounts to values of 0.17, 0.26, 0.28, 0.54, 0.59 for the elements Ba, Si, Mn, Sr, and K, respectively. We suggest that (a) colloidal export likely accounts for the export deficit in Al, Fe, Mn, P, Si, and (b) nutrient uptake and retention in re-growing biomass likely accounts for the export deficit in Ba, K, P, Si, Sr.

With respect to (a) indirect evidence on the neoformation of sub-micron sized particles in the deep regolith and its export with stream water was provided at the SSHCZO (Pennsylvania, USA). For example, Kim et al. (2018) found a discrepancy between the chemistry of stream water (short-term weathering) and regolith (long-term weathering) and also showed that sub-micron sized Al-, Fe-, and Si-rich oxides were found in the suspended sediments of stream water (abundance depends on discharge). However, whether these secondary precipitates were sourced from deep regolith or shallow soil remained unknown. Likewise, at SSHZCO Ma et al. (2015) revealed by means of Mg isotopes, Noireaux et al. (2021) by B isotopes, Sullivan et al. (2016) by Mg, Fe and B isotopes, and Steinhofel et al. (2021) by Li isotopes a missing reservoir in the regolith that they suggested to be caused by loss of sub-micron sized secondary solids. At our Conventwald study site this finding was confirmed by means of Li stable isotopes (Cai et al., 2024). That colloidal-sized particles are generated at deep regolith was shown experimentally by Moravec et al. (2020) on subsamples from a 35 m deep drill core taken from the rhyolitic Jemez River Basin CZO (New Mexico, USA). Other studies have argued for colloid mobilization in the subsurface (DeNovio et al., 2004; McCarthy & McKay, 2004; Ryan & Elimelech, 1996). Given these indirect evidences for colloid formation and transport, we envisage the possibility that at the Conventwald site Al, Fe, P, Si and Mn bearing fine colloids are stored within the unsaturated zone of the saprolite where pores are not constantly hydrologically connected by flowing water. At high flow conditions these pores are hydrologically reconnected to the stream and colloids drain into the stream. This export pathway might represent the unsampled Critical Zone

compartment. To capture this export pathway a sophisticated sampling aperture would be required that allows time series sampling of deep subsurface water without disturbing the subsurface. Unfortunately, to this stage we are lacking of such sampling strategy.

With respect to (b) a biogenic process engineering the export deficit of Ba, K, P, Si, and Sr in deep saprolite is also supported by evidence. The observed 40% deficit found, for example, for K might emerge from deep nutrient uptake and storage in re-growing forest biomass or export in form of plant litter. This suggestion is supported by estimates of the involved fluxes. For example, 40% of  $W_{\text{saprolite}}^{\text{K}}$  amount to a flux of  $\sim 330 \text{ mg m}^{-2} \text{ yr}^{-1}$  that does not end up in the dissolved load but, if not exported as colloids, is available for tree nutrition and storage in re-growing forest biomass or export in form of plant litter. Rough estimates of K loss through litter erosion at our study site amount to  $500 \text{ mg m}^{-2} \text{ yr}^{-1}$  (Uhlig & von Blanckenburg, 2019). The part of this fraction is likely taken up from 2–7 m depth, which is, based on radiogenic Sr isotope ratios and  $^{10}\text{Be}(\text{meteoric})/^{9}\text{Be}$  ratios, the depth section from which mineral nutrients are originally sourced by forest trees at the Conventwald (Uhlig et al., 2020). Even though we lack plant litter export fluxes for Ba and Sr, it is likely that export in biogenic form occurs at our study site, which was demonstrated for Ba in the Amazon (Charbonnier et al., 2020, 2022) and Sr in Chile (Oeser & von Blanckenburg, 2020) as well as by a global erodosequence (Bouchez & von Blanckenburg, 2021).

## 6. Conclusions

From a daily water sampling campaign of six different hydrological compartments within a small watershed, we identified potential causes for differences in chemostatic behavior among different chemical elements; all being in line with previous literature. Whereas chemostasis of atmospheric-sourced Cl is maintained by its chemically passive transit through the watershed, chemostasis of Al and Si is maintained by the formation and dissolution of poorly crystalline secondary solids. Near-chemostatic behavior, or in other words weak dilution behavior, of Ca and Mg is maintained through their large pool in the bioavailable fraction in soil, which has the capacity to buffer Ca and Mg concentrations in the stream. Flushing generates enrichment behavior and chemostatic behavior during periods of high flow of the nutritive element K, dissolved organic carbon (DOC), and trace metals that are either colloidal-bound or complexed with organic matter (Cu, Fe, Zn). Importantly—apart from Cu, DOC, and Fe—flushing is too weak in the Conventwald to cause positive C-Q slopes.

A comparison of short-term element-specific chemical weathering fluxes derived from stream solutions ( $W_{\text{stream}}^{\text{X}}$ ) with long-term element-specific chemical weathering fluxes derived from regolith solids ( $W_{\text{regolith}}^{\text{X}}$ ) reveals deficits in the stream dissolved load and suggests that low frequency high discharge events, such as the flood of the century, are missing in  $W_{\text{stream}}^{\text{X}}$ . These deficits cannot be explained by discharge variation with time, such as an underestimation of modern-day discharge relative to the more humid times of the Holocene period. Rather, deficits found in the stream dissolved load can be attributed to colloidal-bound export for Al, Fe, Mn, P, Si, and particulate biogenic export or retainment in re-growing forest biomass for Ba, K, P, Si, Sr. Disentangling the catchment-wide dissolved export efficiency ( $\text{DEE}_{\text{regolith}}^{\text{X}}$ ) to the dissolved export efficiency from the deep saprolite ( $\text{DEE}_{\text{saprolite}}^{\text{X}}$ ) reveals that deficits found in the stream dissolved load have their origin in the deep saprolite. This finding is consistent with nutrient uptake from the deep saprolite as found in our previous Conventwald studies (Cai et al., 2022; Uhlig et al., 2020; Uhlig & von Blanckenburg, 2019). An unsampled Critical Zone export pathway emerged in multiple Critical Zone studies performed around the globe (von Blanckenburg et al., 2021; Bouchez & von Blanckenburg, 2021; Cai et al., 2024; Charbonnier et al., 2022; Charbonnier et al., 2020; Frings et al., 2021; Kim et al., 2018; Ma et al., 2015; Noireaux et al., 2021; Schuessler et al., 2018; Steinhoefel et al., 2021; Sullivan et al., 2016; Uhlig et al., 2017). Given our indirect evidence for both abiotic and biogenic “hidden” Critical Zone compartment or flux, the deep Critical Zone still warrants attention toward a complete budget of element cycles at the interface of the biosphere, pedosphere, and hydrosphere.

## Data Availability Statement

The data set including Tables S1–S7 of this study is accessible in the data repository under the reference Uhlig et al. (2024).

## Acknowledgments

We are grateful for funding from the German National Science Foundation Priority Program 1685 “Ecosystem nutrition: forest strategies for limited phosphorus resources.” We are also grateful to the Forstliche Versuchsanstalt Baden-Wuerttemberg (FVA) for providing creek discharge and wet atmospheric deposition data. For analytical support we thank Jutta Schlegel. Finally, we are grateful for three constructive reviews from anonymous reviewers and the editor’s comments, which helped to improve the manuscript. Open Access funding enabled and organized by Projekt DEAL.

## References

- Aerts, J. C. J. H., Renssen, H., Ward, P. J., De Moel, H., Odada, E., Bouwer, L. M., & Gooose, H. (2006). Sensitivity of global river discharges under Holocene and future climate conditions. *Geophysical Research Letters*, *33*(19), L19401. <https://doi.org/10.1029/2006GL027493>
- Aguirre, A. A., Derry, L. A., Mills, T. J., & Anderson, S. P. (2017). Colloidal transport in the Gordon Gulch catchment of the Boulder Creek CZO and its effect on C-Q relationships for silicon. *Water Resources Research*, *53*(3), 2368–2383. <https://doi.org/10.1111/j.1752-1688.1969.tb04897.x>
- Bachmaier, S., & Weiler, M. (2012). *Technical report on experimental hillslope hydrology*. Hydronotes, University of Freiburg.
- Bao, C., Li, L., Shi, Y., & Duffy, C. (2017). Understanding watershed hydrogeochemistry: 1. Development of RT-flux-PIHM. *Water Resources Research*, *53*(3), 2328–2345. <https://doi.org/10.1002/2016WR018934>
- Baronas, J. J., Torres, M. A., Clark, K. E., & West, A. J. (2017). Mixing as a driver of temporal variations in river hydrochemistry: 2. Major and trace element concentration dynamics in the Andes-Amazon transition. *Water Resources Research*, *53*(4), 3120–3145. <https://doi.org/10.1002/2016WR019729>
- Barré, P., & Velde, B. (2012). Reversibility of soil forming clay mineral reactions induced by plant – Clay interactions. *EGU*, *14*, 6418.
- Basu, N. B., Destouni, G., Jawitz, J. W., Thompson, S. E., Loukinova, N. V., Darracq, A., et al. (2010). Nutrient loads exported from managed catchments reveal emergent biogeochemical stationarity. *Geophysical Research Letters*, *37*(23), 1–5. <https://doi.org/10.1029/2010GL045168>
- Bern, C. R., Chadwick, O. A., Hartshorn, A. S., Khomo, L. M., & Chorover, J. (2011). A mass-balance model to separate and quantify colloidal and solute redistributions in soil. *Chemical Geology*, *282*(3–4), 113–119. <https://doi.org/10.1016/j.chemgeo.2011.01.014>
- Bern, C. R., Thompson, A., & Chadwick, O. A. (2015). Quantification of colloidal and aqueous element transfer in soils: The dual-phase mass balance model. *Geochimica et Cosmochimica Acta*, *151*, 1–18. <https://doi.org/10.1016/j.gca.2014.12.008>
- Botter, G., Porporato, A., Rodriguez-Iturbe, I., & Rinaldo, A. (2007). Basin-scale soil moisture dynamics and the probabilistic characterization of carrier hydrologic flows: Slow, leaching-prone components of the hydrologic response. *Water Resources Research*, *43*(2). <https://doi.org/10.1029/2006WR005043>
- Bouchez, J., & von Blanckenburg, F. (2021). The role of vegetation in setting strontium stable isotope ratios in the Critical Zone. *American Journal of Science*, *321*(8), 1246–1283. <https://doi.org/10.2475/08.2021.04>
- Brantley, S. L., & Lebedeva, M. (2011). Learning to read the chemistry of regolith to understand the critical zone. *Annual Review of Earth and Planetary Sciences*, *39*(1), 387–416. <https://doi.org/10.1146/annurev-earth-040809-152321>
- Cai, D., Henehan, M. J., Uhlig, D., & von Blanckenburg, F. (2022). Mg isotope composition of runoff is buffered by the regolith exchangeable pool. *Geochimica et Cosmochimica Acta*, *321*(321), 99–114. <https://doi.org/10.1016/j.gca.2022.01.011>
- Cai, D., Henehan, M. J., Uhlig, D., & von Blanckenburg, F. (2024). Lithium isotopes in water and regolith in a deep weathering profile reveal imbalances in Critical Zone fluxes. *Geochimica et Cosmochimica Acta*, *369*, 213–226. <https://doi.org/10.1016/j.gca.2024.01.012>
- Cartwright, I. (2020). Concentration vs. streamflow (C-Q) relationships of major ions in south-eastern Australian rivers: Sources and fluxes of inorganic ions and nutrients. *Applied Geochemistry*, *120*(June), 104680. <https://doi.org/10.1016/j.apgeochem.2020.104680>
- Charbonnier, Q., Bouchez, J., Gaillardet, J., & Gayer, É. (2020). Barium stable isotopes as a fingerprint of biological cycling in the Amazon River basin. *Biogeosciences*, *17*(23), 5989–6015. <https://doi.org/10.5194/bg-17-5989-2020>
- Charbonnier, Q., Bouchez, J., Gaillardet, J., Gayer, E., & Porder, S. (2022). A global imbalance in potassium and barium river export: The result of biological uptake? *Geochemical Perspectives Letters*, *21*, 32–36. <https://doi.org/10.7185/geochemlet.2214>
- Clow, D. W., & Drever, J. I. (1996). Weathering rates as a function of flow through an alpine soil. *Chemical Geology*, *132*(1–4), 131–141. [https://doi.org/10.1016/S0009-2541\(96\)00048-4](https://doi.org/10.1016/S0009-2541(96)00048-4)
- Clow, D. W., & Mast, M. A. (2010). Mechanisms for chemostatic behavior in catchments: Implications for CO<sub>2</sub> consumption by mineral weathering. *Chemical Geology*, *269*(1–2), 40–51. <https://doi.org/10.1016/j.chemgeo.2009.09.014>
- Dawson, T. E., Hahn, W. J., & Crutchfield-Peters, K. (2020). Digging deeper: What the critical zone perspective adds to the study of plant ecophysiology. *New Phytologist*, *226*(3), 666–671. <https://doi.org/10.1111/nph.16410>
- DeNovio, N. M., Saiers, J. E., & Ryan, J. N. (2004). Colloid movement in unsaturated porous media: Recent advances and future directions. *Vadose Zone Journal*, *3*(2), 338–351. <https://doi.org/10.2136/vzj2004.0338>
- Deutscher Wetterdienst. (2021). Retrieved from [https://www.dwd.de/EN/research/observing\\_atmosphere/composition\\_atmosphere/aerosol/cont\\_nav/saharan\\_dust.html](https://www.dwd.de/EN/research/observing_atmosphere/composition_atmosphere/aerosol/cont_nav/saharan_dust.html)
- Dietze, M., & Dietze, E. (2013). EMMAgeo: End-member modelling algorithm and supporting functions for grain-size analysis. *R Package Version*, *0.9*, 1.
- Eichhorn, J., Bolte, A., Chmara, I., Dietrich, H.-P., Fleck, S., Gehrman, J., et al. (2016). Forstliches Umwelt-monitoring in Deutschland Durchführungskonzept Forstliches Umweltmonitoring. Retrieved from [www.bmel.de](http://www.bmel.de)
- Frings, P. J., Schubring, F., Oelze, M., & von Blanckenburg, F. (2021). Quantifying biotic and abiotic Si fluxes in the Critical Zone with Ge/Si ratios along a gradient of erosion rates. *American Journal of Science*, *321*(8), 1204–1245. <https://doi.org/10.2475/08.2021.03>
- Gaillardet, J., Braud, I., Hankard, F., Anquetin, S., Bour, O., Dorfliger, N., et al. (2018). OZCAR: The French network of critical zone observatories. *Vadose Zone Journal*, *17*(1), 1–24. <https://doi.org/10.2136/vzj2018.04.0067>
- Gaillardet, J., Dupré, B., Louvat, P., & Allègre, C. J. (1999). Global silicate weathering and CO consumption rates deduced from the chemistry of large rivers. *Chemical Geology*, *159*(1–4), 3–30. [https://doi.org/10.1016/S0009-2541\(99\)00031-5](https://doi.org/10.1016/S0009-2541(99)00031-5)
- Gibbs, R. J. (1970). Mechanisms controlling world water chemistry. *Science*, *170*(3962), 1088–1090. <https://doi.org/10.1126/science.170.3962.1088>
- Godsey, S. E., Hartmann, J., & Kirchner, J. W. (2019). Catchment chemostasis revisited: Water quality responds differently to variations in weather and climate. *Hydrological Processes*, *33*(24), 3056–3069. <https://doi.org/10.1002/hyp.13554>
- Godsey, S. E., Kirchner, J. W., & Clow, D. W. (2009). Concentration-discharge relationships reflect chemostatic characteristics of US catchments. *Hydrological Processes*, *23*(13), 1844–1864. <https://doi.org/10.1002/hyp.7315>
- Gottselig, N., Sohr, J., Uhlig, D., Nischwitz, V., Weiler, M., & Amelung, W. (2020). Groundwater controls on colloidal transport in forest stream waters. *Science of the Total Environment*, *717*, 134638. <https://doi.org/10.1016/j.scitotenv.2019.134638>
- Herndon, E. M., Dere, A. L., Sullivan, P. L., Norris, D., Reynolds, B., & Brantley, S. L. (2015). Landscape heterogeneity drives contrasting concentration-discharge relationships in shale headwater catchments. *Hydrology and Earth System Sciences*, *19*(8), 3333–3347. <https://doi.org/10.5194/hess-19-3333-2015>
- Hewawasam, T., von Blanckenburg, F., Bouchez, J., Dixon, J. L., Schuessler, J. A., & Maekeler, R. (2013). Slow advance of the weathering front during deep, supply-limited saprolite formation in the tropical Highlands of Sri Lanka. *Geochimica et Cosmochimica Acta*, *118*, 202–230. <https://doi.org/10.1016/j.gca.2013.05.006>

- Hoagland, B., Russo, T. A., Gu, X., Hill, L., Kaye, J., Forsythe, B., & Brantley, S. L. (2017). Hyporheic zone influences on concentration-discharge relationships in a headwater sandstone stream. *Water Resources Research*, 53(6), 4643–4667. <https://doi.org/10.1002/2016WR019717>
- Ibarra, D. E., Caves, J. K., Moon, S., Thomas, D. L., Hartmann, J., Chamberlain, C. P., & Maher, K. (2016). Differential weathering of basaltic and granitic catchments from concentration–discharge relationships. *Geochimica et Cosmochimica Acta*, 190, 265–293. <https://doi.org/10.1016/j.gca.2016.07.006>
- IUSS Working Group WRB. (2015). World reference base for soil resources 2014, update 2015, International soil classification system for naming soils and creating legends for soil maps. World Soil Resources Report 106. Food and Agriculture Organization of the United Nations. <https://doi.org/10.1017/S0014479706394902>
- Jickells, T. D., An, Z. S., Andersen, K. K., Baker, A. R., Bergametti, C., Brooks, N., et al. (2005). Global iron connections between desert dust, ocean biogeochemistry, and climate. *Science*, 308(5718), 67–71. <https://doi.org/10.1126/science.1105959>
- Johnson, N. M., Likens, G. E., Bormann, F. H., Fisher, D. W., & Pierce, R. S. (1969). A working model for the variation in stream water chemistry at the Hubbard brook experimental forest, New Hampshire. *Water Resources Research*, 5(6), 1353–1363. <https://doi.org/10.1029/WR005i006p01353>
- Kabata-Pendias, A. (2011). *Trace elements in soils and plants*. CRC Press. <https://doi.org/10.1201/b10158-25>
- Kim, H., Gu, X., & Brantley, S. L. (2018). Particle fluxes in groundwater change subsurface shale rock chemistry over geologic time. *Earth and Planetary Science Letters*, 500, 180–191. <https://doi.org/10.1016/j.epsl.2018.07.031>
- Kirchner, J. W., & Neal, C. (2013). Universal fractal scaling in stream chemistry and its implications for solute transport and water quality trend detection. *Proceedings of the National Academy of Sciences*, 110(30), 12213–12218. <https://doi.org/10.1073/pnas.1304328110>
- Kretzschmar, R., Robarge, W. P., & Amoozegar, A. (1995). Influence of natural organic matter on colloid transport through saprolite. *Water Resources Research*, 31(3), 435–445. <https://doi.org/10.1029/94wr02676>
- Kump, L. R., Brantley, S. L., & Arthur, M. A. (2000). Chemical weathering, atmospheric CO<sub>2</sub>, and climate. *Annual Review of Earth and Planetary Sciences*, 28(1), 611–667. <https://doi.org/10.1146/annurev.earth.28.1.611>
- Lægdsmand, M., Villholth, K. G., Ullum, M., & Jensen, K. H. (1999). Processes of colloid mobilization and transport in macroporous soil monoliths. *Geoderma*, 93(1–2), 33–59. [https://doi.org/10.1016/S0016-7061\(99\)00041-5](https://doi.org/10.1016/S0016-7061(99)00041-5)
- Lang, F., Krüger, J., Amelung, W., Willbold, S., Frossard, E., Bünemann, E. K., et al. (2017). Soil phosphorus supply controls P nutrition strategies of beech forest ecosystems in Central Europe. *Biogeochemistry*, 136(1), 5–29. <https://doi.org/10.1007/s10533-017-0375-0>
- Ma, L., Teng, F. Z., Jin, L., Ke, S., Yang, W., Gu, H. O., & Brantley, S. L. (2015). Magnesium isotope fractionation during shale weathering in the Shale Hills Critical Zone Observatory: Accumulation of light Mg isotopes in soils by clay mineral transformation. *Chemical Geology*, 397, 37–50. <https://doi.org/10.1016/j.chemgeo.2015.01.010>
- Maher, K. (2010). The dependence of chemical weathering rates on fluid residence time. *Earth and Planetary Science Letters*, 294(1–2), 101–110. <https://doi.org/10.1016/j.epsl.2010.03.010>
- Maher, K. (2011). The role of fluid residence time and topographic scales in determining chemical fluxes from landscapes. *Earth and Planetary Science Letters*, 312(1–2), 48–58. <https://doi.org/10.1016/j.epsl.2011.09.040>
- Maher, K., & Chamberlain, C. P. (2014). Hydrologic regulation of chemical weathering and the geologic carbon cycle. *Science*, 343(6178), 1502–1504. <https://doi.org/10.1126/science.1250770>
- Marschner, P. (2011). Marschner's mineral nutrition of higher plants. <https://doi.org/10.1016/B978-0-12-384905-2.00001-7>
- McCarthy, J. F., & McKay, L. D. (2004). Colloid transport in the subsurface: Past, present, and future challenges. *Vadose Zone Journal*, 3(2), 326–337. <https://doi.org/10.2136/vzj2004.0326>
- McCormick, E. L., Dralle, D. N., Hahn, W. J., Tune, A. K., Schmidt, L. M., Chadwick, K. D., & Rempe, D. M. (2021). Widespread woody plant use of water stored in bedrock. *Nature*, 597(7875), 225–229. <https://doi.org/10.1038/s41586-021-03761-3>
- Miller, M. P., Tesoriero, A. J., Capel, P. D., Pellerin, B., Hyer, K. E., & Burns, D. (2016). Stream fate of nitrate using high-frequency water quality data. *Water Resources Research*, 52(1), 330–347. <https://doi.org/10.1002/2015WR017753>
- Mills, T. J., Anderson, S. P., Bern, C., Aguirre, A., & Derry, L. A. (2017). Colloid mobilization and seasonal variability in a semiarid headwater stream. *Journal of Environmental Quality*, 46(1), 88–95. <https://doi.org/10.2134/jeq2016.07.0268>
- Montgomery, D. R., Brandon, M. T., & Montgomery, D. R. (2002). Topographic controls on erosion rates in tectonically active mountain ranges. *Earth and Planetary Science Letters*, 201(3–4), 481–489. [https://doi.org/10.1016/S0012-821X\(02\)00725-2](https://doi.org/10.1016/S0012-821X(02)00725-2)
- Moon, S., Chamberlain, C. P., & Hilley, G. E. (2014). New estimates of silicate weathering rates and their uncertainties in global rivers. *Geochimica et Cosmochimica Acta*, 134, 257–274. <https://doi.org/10.1016/j.gca.2014.02.033>
- Moravec, B. G., Keifer, V., Root, R. A., White, A. M., Wang, Y., Olshansky, Y., et al. (2020). Experimental weathering of a volcanoclastic critical zone profile: Key role of colloidal constituents in aqueous geochemical response. *Chemical Geology*, 119886, 119886. <https://doi.org/10.1016/j.chemgeo.2020.119886>
- Moravec, B. G., Keifer, V., Root, R. A., White, A. M., Wang, Y., Olshansky, Y., et al. (2021). Experimental weathering of a volcanoclastic critical zone profile: Key role of colloidal constituents in aqueous geochemical response. *Chemical Geology*, 559, 119886. <https://doi.org/10.1016/j.chemgeo.2020.119886>
- Mulholland, P. J. (1992). Regulation of nutrient concentrations in a temperate forest stream: Roles of upland, riparian, and instream processes. *Limnology & Oceanography*, 37(7), 1512–1526. <https://doi.org/10.4319/lo.1992.37.7.1512>
- Musolff, A., Schmidt, C., Selle, B., & Fleckenstein, J. H. (2015). Catchment controls on solute export. *Advances in Water Resources*, 86, 133–146. <https://doi.org/10.1016/j.advwatres.2015.09.026>
- Noireaux, J., Sullivan, P. L., Gaillardet, J., Louvat, P., Steinhöfel, G., & Brantley, S. L. (2021). Developing boron isotopes to elucidate shale weathering in the critical zone. *Chemical Geology*, 559, 119900. <https://doi.org/10.1016/j.chemgeo.2020.119900>
- Oeser, R. A., & von Blanckenburg, F. (2020). Strontium isotopes trace biological activity in the Critical Zone along a climate and vegetation gradient. *Chemical Geology*, 558(June), 119861. <https://doi.org/10.1016/j.chemgeo.2020.119861>
- Pacific, V. J., Jencso, K. G., & McGlynn, B. L. (2010). Variable flushing mechanisms and landscape structure control stream DOC export during snowmelt in a set of nested catchments. *Biogeochemistry*, 99(1), 193–211. <https://doi.org/10.1007/s10533-009-9401-1>
- Parkhurst, D. L., & Appelo, C. A. J. (2013). Description of input and examples for PHREEQC version 3 — A computer program for speciation, batch-reaction, *One-dimensional transport, and inverse geochemical calculations*. : U.S. Geological Survey. <https://doi.org/10.3133/tm6A43>
- Rempe, D. M., & Dietrich, W. E. (2018). Direct observations of rock moisture, a hidden component of the hydrologic cycle. In *Proceedings of the national academy of sciences* (pp. 1–6). <https://doi.org/10.1073/pnas.1800141115>
- Ryan, J. N., & Elimelech, M. (1996). Colloid mobilization and transport in groundwater. *Colloids and Surfaces A. Physicochemical and Engineering Aspects*, 107(95), 1–56. [https://doi.org/10.1016/0927-7757\(95\)03384-X](https://doi.org/10.1016/0927-7757(95)03384-X)



- Schuessler, J. A., Kämpf, H., Koch, U., & Alawi, M. (2016). Earthquake impact on iron isotope signatures recorded in mineral spring water. *Journal of Geophysical Research: Solid Earth*, *121*(12), 8548–8568. <https://doi.org/10.1002/2016JB013408>
- Schuessler, J. A., von Blanckenburg, F., Bouchez, J., Uhlig, D., & Hewawasam, T. (2018). Nutrient cycling in a tropical montane rainforest under a supply-limited weathering regime traced by elemental mass balances and Mg stable isotopes. *Chemical Geology*, *497*, 74–87. <https://doi.org/10.1016/j.chemgeo.2018.08.024>
- Seibert, J., Grabs, T., Köhler, S., Laudon, H., Winterdahl, M., & Bishop, K. (2009). Linking soil- and stream-water chemistry based on a riparian flow-concentration integration model. *Hydrology and Earth System Sciences*, *13*(12), 2287–2297. <https://doi.org/10.5194/hess-13-2287-2009>
- Sohrt, J., Uhlig, D., Kaiser, K., Blanckenburg, F. V., Siemens, J., Seeger, S., et al. (2019). Phosphorus fluxes in a temperate forested watershed: Canopy leaching, runoff sources, and in-stream transformation. *Frontiers in Forests and Global Change*, *2*(December), 1–14. <https://doi.org/10.3389/ffgc.2019.00085>
- Steinhöfel, G., Brantley, S. L., & Fantle, M. S. (2021). Lithium isotopic fractionation during weathering and erosion of shale. *Geochimica et Cosmochimica Acta*, *295*, 155–177. <https://doi.org/10.1016/j.gca.2020.12.006>
- Sullivan, P. L., Goddérís, Y., Shi, Y., Gu, X., Schott, J., Hasenmueller, E. A., et al. (2019). Exploring the effect of aspect to inform future earthcasts of climate-driven changes in weathering of shale. *Journal of Geophysical Research: Earth Surface*, *124*(4), 974–993. <https://doi.org/10.1029/2017JF004556>
- Sullivan, P. L., Ma, L., West, N., Jin, L., Karwan, D. L., Noireaux, J., et al. (2016). CZ-tope at Susquehanna Shale Hills CZO: Synthesizing multiple isotope proxies to elucidate Critical Zone processes across timescales in a temperate forested landscape. *Chemical Geology*, *445*, 103–119. <https://doi.org/10.1016/j.chemgeo.2016.05.012>
- Taylor, S. R., & McLennan, S. M. (1995). The geochemical evolution of the continental crust. *Reviews of Geophysics*, *33*(2), 241–265. <https://doi.org/10.1029/95RG00262>
- Thomas, Z., Abbott, B. W., Troccaz, O., Baudry, J., & Pinay, G. (2016). Proximate and ultimate controls on carbon and nutrient dynamics of small agricultural catchments. *Biogeosciences*, *13*(6), 1863–1875. <https://doi.org/10.5194/bg-13-1863-2016>
- Thompson, S. E., Basu, N. B., Lascrain, J., Aubeneau, A., & Rao, P. S. C. (2011). Relative dominance of hydrologic versus biogeochemical factors on solute export across impact gradients. *Water Resources Research*, *47*(7), 1–20. <https://doi.org/10.1029/2010WR009605>
- Tipper, E. T., Stevenson, E. I., Alcock, V., Knight, A. C. G., Baronas, J. J., Hilton, R. G., et al. (2021). Global silicate weathering flux overestimated because of sediment-water cation exchange. *Proceedings of the National Academy of Sciences of the United States of America*, *118*(1), 1–6. <https://doi.org/10.1073/pnas.2016430118>
- Torres, M., Joshua West, A., & Clark, K. E. (2015). Geomorphic regime modulates hydrologic control of chemical weathering in the Andes-Amazon. *Geochimica et Cosmochimica Acta*, *166*, 105–128. <https://doi.org/10.1016/j.gca.2015.06.007>
- Trostle, K. D., Ray Runyon, J., Pohlmann, M. A., Redfield, S. E., Pelletier, J., McIntosh, J., & Chorover, J. (2016). Colloids and organic matter complexation control trace metal concentration-discharge relationships in Marshall Gulch stream waters. *Water Resources Research*, *52*(10), 7931–7944. <https://doi.org/10.1002/2016WR019072>
- Tune, A. K., Druhan, J. L., Wang, J., Bennett, P. C., & Rempe, D. M. (2020). Carbon dioxide production in bedrock beneath soils substantially contributes to forest carbon cycling. *Journal of Geophysical Research: Biogeosciences*, *125*(12). <https://doi.org/10.1029/2020JG005795>
- Uhlig, D., Amelung, W., & von Blanckenburg, F. (2020). Mineral nutrients sourced in deep regolith sustain long-term nutrition of mountainous temperate forest ecosystems. *Global Biogeochemical Cycles*, *34*(9), 1–21. <https://doi.org/10.1029/2019GB006513>
- Uhlig, D., Schuessler, J. A., Bouchez, J., Dixon, J. L., & von Blanckenburg, F. (2017). Quantifying nutrient uptake as driver of rock weathering in forest ecosystems by magnesium stable isotopes. *Biogeosciences*, *14*(12), 3111–3128. <https://doi.org/10.5194/bg-14-3111-2017>
- Uhlig, D., Sohrt, J., & von Blanckenburg, F. (2024). Major and trace element concentrations in Critical Zone water compartments in the Conventwald [Dataset]. *GFZ Data Services*. <https://doi.org/10.5880/figeo.2023.020>
- Uhlig, D., & von Blanckenburg, F. (2019). How slow rock weathering balances nutrient loss during fast forest floor turnover in montane, temperate forest ecosystems. *Frontiers in Earth Science*, *7*(July), 1–28. <https://doi.org/10.3389/feart.2019.00159>
- Vallejo-Bernal, S. M., Ramírez, J. M., & Poveda, G. (2021). A conceptual stochastic rainfall-runoff model of an order-one catchment under a stationary precipitation regime. *Stochastic Environmental Research and Risk Assessment*, *35*(11), 2187–2212. <https://doi.org/10.1007/s00477-021-02041-w>
- Vitousek, P. M. (1977). The regulation of element concentrations in mountain streams in the northeastern United States. *Ecological Monographs*, *47*(1), 65–87. <https://doi.org/10.2307/1942224>
- von Blanckenburg, F., Schuessler, J. A., Bouchez, J., Frings, P. J., Uhlig, D., Oelze, M., et al. (2021). Rock weathering and nutrient cycling along an erodosequence. *American Journal of Science*, *321*(8), 1111–1163. <https://doi.org/10.1126/science.5.127.888>
- von Blanckenburg, F., Wittmann, H., & Schuessler, J. A. (2016). HELGES: Helmholtz laboratory for the geochemistry of the Earth surface. *Journal of Large-Scale Research Facilities*, *2*, 1–5. <https://doi.org/10.17815/jlsrf-2-141>
- White, A. F., & Blum, A. E. (1995). Effects of climate on chemical weathering in watersheds. *Geochimica et Cosmochimica Acta*, *59*(9), 1729–1747. [https://doi.org/10.1016/0016-7037\(95\)00078-e](https://doi.org/10.1016/0016-7037(95)00078-e)
- Wilkinson, B. H. (2015). Precipitation as meteoric sediment and scaling laws of bedrock incision: Assessing the sadler effect. *The Journal of Geology*, *123*(2), 95–112. <https://doi.org/10.1086/681588>
- Winnick, M. J., Carroll, R. W. H., Williams, K. H., Maxwell, R. M., Dong, W., & Maher, K. (2017). Snowmelt controls on concentration-discharge relationships and the balance of oxidative and acid-base weathering fluxes in an alpine catchment, East River, Colorado. *Water Resources Research*, *53*(3), 2507–2523. <https://doi.org/10.1002/2016WR019724>
- Zakharova, E. A., Pokrovsky, O. S., Dupré, B., & Zaslavskaya, M. B. (2005). Chemical weathering of silicate rocks in Aldan Shield and Baikal Uplift: Insights from long-term seasonal measurements of solute fluxes in rivers. *Chemical Geology*, *214*(3–4), 223–248. <https://doi.org/10.1016/j.chemgeo.2004.10.003>
- Zender, C. S., Bian, H., & Newman, D. (2003). Mineral dust entrainment and deposition (DEAD) model: Description and 1990s dust climatology. *Journal of Geophysical Research: Atmospheres*, *108*(14). <https://doi.org/10.1029/2002jd002775>
- Zhang, W., Tang, X. Y., Weisbrod, N., Zhao, P., & Reid, B. J. (2015). A coupled field study of subsurface fracture flow and colloid transport. *Journal of Hydrology*, *524*, 476–488. <https://doi.org/10.1016/j.jhydrol.2015.03.001>
- Zhi, W., Li, L., Dong, W., Brown, W., Kaye, J., Steefel, C., & Williams, K. H. (2019). Distinct source water chemistry shapes contrasting concentration-discharge patterns. *Water Resources Research*, *55*(5), 4233–4251. <https://doi.org/10.1029/2018WR024257>
- Zirkler, D., Lang, F., & Kaupenjohann, M. (2012). “Lost in filtration” - The separation of soil colloids from larger particles. *Colloids and Surfaces A. Physicochemical and Engineering Aspects*, *399*, 35–40. <https://doi.org/10.1016/j.colsurfa.2012.02.021>